

1 **Optimization of Biological Production for Indian Ocean upwelling zones: Part – I:**

2 **Improving Biological Parameterization via a variable Compensation Depth**

3

4 Mohanan Geethalekshmi Sreeush^{1,2,*}.

5 Vinu Valsala¹,

6 Sreenivas Pentakota¹,

7 Koneru Venkata Siva Rama Prasad²,

8 Raghu Murtugudde³

9

10 ¹Indian Institute of Tropical Meteorology, Pune, India

11 ²Department of Meteorology and Oceanography, Andhra University, India

12 ³ESSIC, University of Maryland, USA

13

14 *(Under revision BGD)*

15

16 *Corresponding author address:

17 Indian Institute of Tropical Meteorology,

18 Dr. Homi Bhabha Road, Pashan, Pune 411 008, India

19 E-Mail: sreeushmg@tropmet.res.in

20

21 **Abstract**

22

23 Biological modeling approach adopted by the Ocean Carbon-cycle Model Inter-comparison
24 Project (OCMIP-II) provided amazingly simple but surprisingly accurate rendition of the annual
25 mean carbon cycle for the global ocean. Nonetheless, OCMIP models are known to have
26 seasonal biases which are typically attributed to their bulk parameterization of ‘compensation
27 depth’. Utilizing the criteria of surface Chl-a based attenuation of solar radiation and the
28 minimum solar radiation required for production, we have proposed a new parameterization for a
29 spatially and temporally varying ‘compensation depth’ which captures the seasonality in the
30 production zone reasonably well. This new parameterization is shown to improve the seasonality
31 of CO₂ fluxes, surface ocean pCO₂, biological export and new production in the major upwelling
32 zones of the Indian Ocean. The seasonally varying compensation depth enriches the nutrient
33 concentration in the upper ocean yielding more faithful biological exports which in turn leads to
34 an accurate seasonality in the carbon cycle. The export production strengthens by ~70% over the
35 western Arabian Sea during monsoon period and achieves a good balance between export and
36 new production in the model. This underscores the importance of having a seasonal balance in
37 model export and new productions for a better representation of the seasonality of carbon cycle
38 over upwelling regions. The study also implies that both the biological and solubility pumps play
39 an important role in the Indian Ocean upwelling zones.

40

41 Keywords: Indian Ocean upwelling zones, Carbon cycle, Seasonal cycle - CO₂ flux and Oceanic
42 pCO₂, Biogeochemical model parameterization, Export production - New production balance,
43 Solubility and Biological pump.

44

45 **1. Introduction**

46 The Indian Ocean is characterized by the unique seasonally reversing monsoon wind systems
47 which act as the major physical drivers for the coastal and open ocean upwelling processes. The
48 major upwelling systems in the Indian Ocean are (1) the western Arabian Sea (WAS; Ryther and
49 Menzel, 1965; Smith et al., 2001; Sarma, 2004; Wiggert et al., 2005, 2006; Murtugudde et al.,
50 2007; McCreary et al., 2009; Prasanna Kumar et al., 2010; Naqvi et al., 2010; Roxy et al., 2015)
51 (2) the Sri Lanka Dome (SLD; Vinayachandran et al., 1998, 2004), (3) Java and Sumatra coasts
52 (SC; Murtugudde et al., 1999; Susanto et al., 2001; Osawa et al., 2010; Xing et al., 2012) and (4)
53 the Seychelles-Chagos thermocline ridge (SCTR; Murtugudde et al., 1999; Dilmahamod et al.,
54 2016, Figure 1). The physical and biological processes and their variability over these key
55 regions are inseparably tied to the strength of the monsoon winds and associated nutrient
56 dynamics. The production and its variability over these coastal upwelling systems are a key
57 concern for the fishing community, since they affect the day-to-day livelihood of the coastal
58 populations (Harvell et al., 1999; Roxy et al., 2015; Praveen et al., 2016) and are important for
59 the Indian Ocean rim countries due to their developing country status.

60 Arabian Sea is a highly productive coastal upwelling system characterized by phytoplankton
61 blooms both in summer (Prasanna Kumar et al., 2001; Naqvi et al., 2003; Wiggert et al., 2005)
62 and winter (Banse and McClain, 1986; Wiggert et al., 2000; Barber et al., 2001; Prasannakumar
63 et al., 2001; Sarma, 2004). The Arabian Sea is known for the second largest Tuna fishing region
64 in the Indian Ocean (Lee et al., 2005). The Somali and Omani upwelling regions experience
65 phytoplankton blooms that are prominent with Net Primary Production (NPP) exceeding 435 g C
66 m⁻² yr⁻¹ (Liao et al., 2016). On the other hand productivity over the SLD (Vinayachandran and
67 Yamagata, 1998) is triggered by open ocean Ekman suction with strong Chl-a blooms during the

68 summer monsoon (Murtugudde et al., 1999; Vinayachandran et al., 2004). Similarly, the SC
69 upwelling is basically due to the strong alongshore winds and its variation is associated with the
70 impact of equatorial and coastal Kelvin waves (Murtugudde et al., 2000, Valsala and Rao, 2016).
71 The interannual variability associated with the Java-Sumatra coastal upwelling is strongly
72 coupled with ENSO (El-Niño Southern Oscillation) through the Walker cell and Indonesian
73 throughflow (Susanto et al., 2001; Valsala et al., 2011) and peaks in July through August with a
74 potential new production of 0.1 Pg C yr^{-1} (Xing et al., 2012). The SCTR productivity has a large
75 spatial and interannual variability. The warmer upper ocean condition associated with El Niño
76 reduces the amplitude of subseasonal SST variability over the SCTR (Jung and Kirtman., 2016).
77 The Chl-a concentration peaks in summer when the southeast trade winds induce mixing and
78 initiate the upwelling of nutrient-rich water (Murtugudde et al., 1999; Wiggert et al., 2006;
79 Vialard et al., 2009; Dilmahamod et al., 2016).

80 Understanding the biological production and variability in the upwelling systems is important
81 because it gives us crucial information regarding marine ecosystem variability (Colwell, 1996;
82 Harvell et al., 1999). The observations also provide vital insights into physical and biological
83 interactions of the ecosystem (Naqvi et al., 2010) as well as the biophysical feedbacks
84 (Murtugudde et al., 2001), although limitations of sparse observations often force us to depend
85 on models to examine the large spatio-temporal variability of the ecosystem (Valsala et al.,
86 2013). Simple to intermediate complexity marine ecosystem models have been employed by
87 several of the previous studies (Sarmiento et al., 2000; Orr et al., 2001; Matsumoto et al., 2008).
88 However, the representation of marine ecosystem with proper parameterizations in models has
89 always been a daunting task. This is an impediment to the accurate representation of biological

90 primary and export productions in models (Friedrichs et al., 2006, 2007) and these issues also
91 impact the modeling of upper trophic levels (Lehodey et al., 2010).

92 Biological production can be quantified with a better understanding of primary production
93 which depends on water temperature, light and nutrient availability (Brock et al., 1993; Moisan
94 et al., 2002) and this became the key reason for parameterizing the production in models as one
95 or more combinations of these terms (Yamanaka et al., 2004). Any of these basic parameters can
96 be tweaked to alter production in models. For example, the availability of nutrients and light
97 determines the phytoplankton growth (Eppely et al., 1972) or growth rate (Boyd et al., 2013).
98 Stoichiometry and carbon-to-Chl-a ratios are other important factors to be considered in
99 modeling (Christian et al., 2001, Wang et al., 2009) but we will not consider them in this study.

100 The Ocean Carbon-cycle Model Intercomparison Project (OCMIP) greatly improved our
101 understanding of global carbon cycle (Najjar and Orr, 1998). OCMIP-II further introduced a
102 simple phosphate-dependent production term in biological models for long-term simulations of
103 the carbon cycle in response to anthropogenic climate change with an accurate annual mean state
104 (Najjar and Orr, 1998; Orr et al., 2001; Doney et al., 2004). However, the OCMIP – II model
105 simulations come with a penalty of strong seasonal biases when compared with observations
106 (Orr et al., 2003). In this protocol, the community compensation depth (hereinafter Z_c) is defined
107 as the depth at which photosynthesis equals entire community respiration and the irradiance at
108 which this balance is achieved is the compensation irradiance (E_{com}). Note that Z_c is clearly
109 different from the conventional euphotic zone depth (Morel, 1988). At Z_c , the Net Community
110 Production is zero and above Z_c the NPP exceeds the community respiration and the ecosystem
111 will grow (Smetacek and Passow, 1990; Gattuso et al., 2006; Sarmiento and Gruber, 2006;
112 Regaudix-de-Gioux and Duarte, 2010; Marra et al., 2014). Therefore the region above Z_c

113 represents the production zone in this modeling approach. However, Z_c was held constant in
114 time and space in OCMIP-II models (Najjar and Orr, 1998; Matsumoto et al., 2008) because the
115 OCMIP-II protocol takes the minimalistic approach to biology and simplifies the model
116 calculations with a very limited set of state variables suitable for long term simulations when
117 casted in coarse resolution models (Orr et al., 2005). Though in reality Z_c varies in space and
118 time (Najjar and Keeling, 1997) just as the euphotic zone depth does as documented in ship
119 measurements (Qasim, 1977, 1982). The variation in Z_c indicates the seasonality of the
120 production zone itself.

121 Most of the biophysical models prescribe a constant value for Z_c , e.g., a default value of
122 $Z_c = 75$ m in OCMIP –II protocol (Najjar and Orr, 1998) and $Z_c = 100$ m in Minnesota Earth
123 System Model (Matsumoto et al., 2008). Depending on the latitude, Z_c varies between 50m and
124 100m in the real world (Najjar and Keeling, 1997). In our study we have attempted a novel
125 biological parameterization scheme for spatially and temporally varying Z_c in the OCMIP–II
126 framework by representing the production as a function of solar radiation (Parsons et al., 1984)
127 and prescribed Chl-a. In this hypothesis, a spatially and temporally varying Z_c is estimated from
128 the vertical attenuation of insolation by the surface Chl-a. The depth at which the insolation
129 reaches the compensation irradiance (chosen as 10 Wm^{-2}) is taken as Z_c . Phosphorous is the
130 basic currency which limits the production within this varying Z_c . This spatially and temporally
131 varying Z_c represents the seasonality in the production zone which is lacking in the original
132 OCMIP-II protocol.

133 Regions of sustained upwelling like the eastern equatorial Pacific are well understood in
134 terms of the role of upwelling in increasing the surface water $p\text{CO}_2$ to drive an outgassing of CO_2
135 into the atmosphere (Feely et al., 2001; Valsala et al., 2014). The Indian Ocean on the other hand

136 experiences only seasonal upwelling which is relatively weak in the deep tropics but stronger off
137 the coasts of Somalia and Oman and in the SLD (Valsala et al., 2013). The relative importance of
138 the solubility vs. biological pump is not well understood. Our focus here on implementing
139 seasonality in Z_c of OCMIP models nonetheless leads to new insights on the impact of improved
140 biological production on surface water $p\text{CO}_2$ and air-sea CO_2 fluxes. The improvements due to
141 the effect of a variable Z_c over the Indian Ocean and the sensitivity experiments where
142 upwelling is muted strongly imply that the biological pump may play as much of a role as the
143 solubility pump in determining surface $p\text{CO}_2$ and CO_2 fluxes over the Indian Ocean.

144 The paper is organized as follows. Model, Data, and Methods are detailed in Section 2.
145 The spatially inhomogeneous Z_c derived out of the new parameterization and its impact on
146 simulated seasonality of biology and carbon cycle are detailed in Section 3. Further results and
147 discussion are followed in Section 4 and a conclusion is given in Section 5.

148

149 **2. Model, Data, and Methods**

150 **2.1. Model**

151 The study utilizes the Offline Ocean Tracer Transport Model (OTTM; Valsala et al., 2008)
152 coupled with OCMIP biogeochemistry model (Najjar and Orr, 1998). OTTM does not compute
153 currents and stratifications (i.e., temperature and salinity) on its own. It is capable of accepting
154 any ocean model or data-assimilated product as physical drivers. The physical drivers prescribed
155 include 4-dimensional currents (u,v), temperature, salinity, and 3-dimensional mixed layer depth,
156 surface freshwater and heat fluxes, surface wind stress and sea surface height. The resolution of
157 the model setup is similar to the parent model from which it borrows the physical drivers. With

158 the given input of Geophysical Fluid Dynamics Laboratory (GFDL) reanalysis data (Chang et.
 159 al., 2012), the zonal and meridional resolutions are 1° with 360 grid points longitudinally and 1°
 160 at higher latitudes but having a finer resolution of 0.8° in the tropics, with 200 latitudinal grid
 161 points. The model has 50 vertical levels with 10m increment in the upper 225m and stretched
 162 vertical levels below 225m. The horizontal grids are formulated in spherical coordinates and
 163 vertical grids are in z levels. The model employs a B-grid structure in which the velocities are
 164 resolved at corners of the tracer grids. The model uses a centered-in-space and centered-in-time
 165 (CSCT) numerical scheme along with an Asselin-Robert filter (Asselin, 1972) to control the
 166 ripples in CSCT.

167 The tracer concentration (C) evolves with time as

$$168 \quad \frac{\partial C}{\partial t} + U \cdot \nabla_H C + W \frac{\partial C}{\partial z} = \frac{\partial}{\partial z} K_z \frac{\partial C}{\partial z} + \nabla_H \cdot (K_h \nabla_H C) + J + F \quad (1)$$

169 where ∇_H is the horizontal gradient operator, U and W are the horizontal and vertical velocities
 170 respectively. K_z is the vertical mixing coefficient, and K_h is the two-dimensional diffusion
 171 tensor. J represents any sink or source due to the internal consumption or production of the
 172 tracer. F represents the emission or absorption of fluxes at the ocean surface. Here, the source
 173 and sink terms are provided through the biogeochemical model. Vertical mixing is resolved in
 174 the model using K- profile parameterization (KPP) (Large et al., 1994).

175 In addition to KPP, the model uses a background vertical diffusion reported by Bryan and Lewis
 176 (Bryan and Lewis, 1979). For horizontal mixing, model incorporates Redi fluxes (Redi, 1982)
 177 and GM fluxes (Gent and McWilliams, 1990) which represent the eddy-induced variance in the
 178 mean tracer transport. A weak Laplacian diffusion is also included in the model for
 179 computational stability where the sharp gradient in concentration occurs.

180 2.2. Biogeochemical model

181 The biogeochemical model used in the study is based on the OCMIP – II protocol as
182 stated above. The main motivation of OCMIP–II protocol is to employ a minimalistic approach
183 to simulate the ocean carbon cycle with a nutrient restoration approach to calculate the oceanic
184 biological production (Najjar et al., 1992; Anderson and Sarmiento, 1995). The present version
185 of the model has four prognostic variables coupled with the circulation field, viz., inorganic
186 phosphate (PO_4^{3-}), dissolved organic phosphorus (DOP), dissolved inorganic carbon (DIC) and
187 alkalinity (ALK). The basic currency for the biological model is phosphorous because of the
188 availability of a more extensive phosphate database and to eliminate the complexities associated
189 with nitrogen fixation and denitrification.

190 The production of organic phosphorus in the model using the nutrient restoring approach is given
191 by

$$192 J_{prod} = \frac{1}{\tau} ([PO_4] - [PO_4]^*) \quad (2)$$

$$193 [PO_4] > [PO_4]^* ; Z < Z_c$$

$$194 J_{prod} = 0 \quad (3)$$

$$195 [PO_4] \leq [PO_4]^* ; Z > Z_c$$

196 Where $[PO_4]^*$ is the observed phosphate concentration and $\tau=30$ days is the restoration time scale
197 (Najjar et. al., 1992).

198 The vertically integrated new production ($g C m^{-2} yr^{-1}$) in the model is defined as

199
$$\text{New production} = \int_{z_c}^0 -J_{prod} dz \quad (4)$$

200 The export production ($\text{g C m}^{-2} \text{ yr}^{-1}$) in the model is calculated as given below

201
$$\text{Export production} = (1 - \sigma) \int_0^{z_c} J_{prod} dz \quad (5)$$

202 Air-sea CO_2 flux in the model is estimated by,

203
$$F = K_w \Delta p\text{CO}_2 \quad (6)$$

204 where K_w is gas transfer velocity and $\Delta p\text{CO}_2$ is the difference in partial pressure of carbon
 205 dioxide between the ocean and atmosphere.

206 $p\text{CO}_2$ is calculated in the model by using DIC and ALK and is given by,

207
$$p\text{CO}_2 = \frac{[\text{DIC}]}{K_0} \frac{[H^+]^2}{[H^+]^2 + K_1[H^+] + K_1K_2} \quad (7)$$

208 Where $[H^+]$ is calculated using Newton-Raphson iterative method (Press et. al., 1996, Najjar and
 209 Orr, 1998). K_0 is the solubility constant of CO_2 and K_1, K_2 are the dissociation constant for
 210 carbonic acid respectively (Sarmiento and Gruber, 2006, Weiss, 1974, Mehrbach et al., 1973,
 211 Dickson and Millero, 1987, Najjar and Orr, 1998).

212 Details of all parameters in the biogeochemical model and calculations of solubility and
 213 biological pump are provided in Appendix-A. The design and validation of the physical model is
 214 reported by Valsala et al., (2008, 2010) and biogeochemical model by Najjar and Orr (1998).

215

216 **2.3. Data**

217 For validating the model results, observational datasets of CO₂ flux and pCO₂ are taken
218 from Takahashi et al., (2009). Satellite-derived Net Primary Production (NPP) data were taken
219 from Sea-viewing Wide Field of view Sensor (SeaWiFS) Chl-a product, calculated using
220 Vertically Generalized Production Model (VGPM) (Behrenfeld and Falkowski, 1997). The NPP
221 data is scaled to export production (EP) by multiplying with an e-ratio ($e = 0.37$) representative
222 of Indian Ocean upwelling zones (Sarmiento and Gruber, 2006, Laws et al., 2000; Falkowski et
223 al., 2003). The initial conditions for PO₄ are taken from the World Ocean Atlas (Garcia et al.,
224 2014). Initial conditions for DIC and ALK are taken from the Global Ocean Data Analysis
225 Project (GLODAP; Key et al., 2004) dataset. The dissolved Organic Phosphorous (DOP) is
226 initialized with a constant value of 0.02 $\mu\text{mol kg}^{-1}$ (Najjar and Orr, 1998). The data sources and
227 citations are provided in the Acknowledgement.

228

229 **2.4. Methods**

230 A spin-up for 50 years from the given initial conditions is performed with the
231 climatological physical drivers. As the initial conditions are provided from a mean state of
232 observed climatology this duration of spin-up is sufficient to reach statistical equilibrium in the
233 upper 1000 m (Le Quere et al., 2000). Atmospheric pCO₂ has been set to a value from the 1950s
234 in the spin-up run for calculating the air-sea CO₂ exchange. A seasonal cycle of atmospheric
235 pCO₂ has been prescribed as in Keeling et al. (1995).

236 After the spin-up, an interannual simulation for 50 years from 1961 to 2010 has been
237 carried out with the corresponding observed atmospheric pCO₂ described in Keeling et al.,
238 (1995). The first five years of the interannual run were looped five times through the physical

239 fields of 1961 repeatedly for a smooth merging of the spin-up restart to the interannual physical
240 variables. Since the study is focused on bias corrections to the seasonal cycle of pCO₂ and DIC
241 with a variable Z_c, a model climatology for carbon cycle has been constructed from 1990 to
242 2010, which includes the anthropogenic increase of oceanic DIC in the climatological calculation
243 and is comparable with the Takahashi et al. (2009) observations.

244 Additional two sensitivity experiments have been performed separately by providing
245 annual mean currents or temperatures as drivers over selected regions of the basin in order to
246 segregate the role of varying Z_c in improving the seasonality of carbon cycle. The aim of these
247 sensitivity experiments is to understand how successful the new parameterization for Z_c is in
248 capturing the carbon cycle variability related to the upwelling episodes even though the seasonal
249 cycle in physics is suppressed. The model driven with annual mean currents suppresses the
250 effect of upwelling by muting the Ekman divergence over the region of interest. On the other
251 hand, the model forced with annual mean temperatures suppresses the cooling effect of
252 upwelling. A smoothing technique with linear interpolation ($u = u(1 - x) + \bar{u}x$) is applied to
253 the offline-data in order to blend the annual mean fields (\bar{u}) provided to the selected region with
254 the rest of the domain (u) in order to reduce a sudden transition at the boundaries. Here x
255 represents an index which varies between 0 and 1 within a distance of 10⁰ from the boundaries of
256 the region of interest to the rest of the model domain.

257

258 **2.5. Community compensation depth (Z_c) parameterization**

259 The OCMIP – II protocol separates the production and consumption zones by a depth termed
260 as compensation depth (Z_c); the depth at which photosynthesis is large enough to balance the

261 community respiration (i.e., both the autotrophic and heterotrophic respiration). At the
262 community compensation depth, the Net Community Production (NCP) is zero i.e., $NCP = NPP$
263 $- R_h = 0$, where NPP is Net Primary Production (i.e., $NPP = GPP - R_a$), GPP is gross primary
264 production, and R_h and R_a are the heterotrophic and autotrophic respirations, respectively
265 (Smetacek and Passow, 1990; Najjar and Orr, 1998; Gattuso et al., 2006; Regaudix-de-Gioux
266 and Duarte, 2010; Marra et al., 2014). The light intensity at Z_c is compensation irradiance (E_{com}),
267 the irradiance at which the gross community primary production balances respiratory carbon
268 losses for the entire community (Gattuso et al., 2006; Regaudix-de-Gioux and Duarte, 2010). We
269 define a spatially and temporally varying compensation depth (hereinafter $varZ_c$) as a depth
270 where compensation irradiance (attenuated by surface Chl-a, Jerlov et al., 1976) reaches a
271 minimum value of 10 W m^{-2} . In this way, the $varZ_c$ has both spatio-temporal variability of light
272 as well as Chl-a. The Chl-a is given as monthly climatology as constructed from satellite data.
273 Observations show that the primary production reduces rapidly to 20% or less of the surface
274 value below a threshold of 10 W m^{-2} (Parsons et al., 1984; Ryther, 1956; Sarmiento and Gruber,
275 2006). Moreover higher ocean temperatures (those in the tropics) enhance the respiration rates
276 resulting in high compensation irradiance (Parsons et al., 1984; Ryther, 1956; Lopez-Urrutia et
277 al., 2006; Regaudix-de-Gioux and Duarte, 2010). A study by Regaudix-de-Gioux and Duarte
278 (2010) reported the mean value of compensation irradiance over the Arabian Sea as 0.4 ± 0.2
279 $\text{mol photon m}^{-2} \text{ day}^{-1}$ which is close to $10 \text{ W m}^{-2} \text{ day}^{-1}$.

280 Figure 2 compares the scatter of average relative photosynthesis within $varZ_c$ as a
281 function of solar radiation for the Indian Ocean (see Appendix-B). This encapsulates the
282 corresponding curve from the observations for the major phytoplankton species in the ocean such
283 as diatoms, green algae and dinoflagellates (Ryther et al., 1956; Parsons et al., 1984; Sarmiento

284 and Gruber, 2006). The model permits 100% production of organic phosphorus for radiation
285 above 50 W m^{-2} . However the availability of phosphate concentration in the model acts as an
286 additional limit for production which indirectly represents the photoinhibition at higher
287 irradiance; for example, in the oligotrophic gyres.

288

289 3. Results and Discussions

290 The inclusion of seasonality in Zc by way of parameterizing varZc leads to a remarkable
291 spatio-temporal variability in Zc (Figure 3). Zc over the Arabian Sea varies from 10 m to 25 m
292 during December to February (DJF) and deepens down to 45 m during March to May (MAM)
293 due to the increase in the surface solar radiation. During the monsoon season i.e., June to
294 September (JJAS), Zc again shoals to 10 m - 35 m due to the attenuation of solar radiation by the
295 increased biological production (Chl-a). During October to November (OCT-NOV), Zc slightly
296 deepens as compared to JJAS.

297 The Bay of Bengal Zc deepens from 35 m to 40 m during DJF and further deepens to 50 m
298 during MAM when the solar radiation is maximum and biological production is minimum
299 (Prasannakumar et al., 2002). Further reduction of Zc can be seen through JJAS as a result of a
300 reduction in solar radiation during monsoon cloud cover. Zc during OCT-NOV is 35 m on
301 average.

302 The equatorial Indian Ocean can be seen as a belt of 40 m - 45 m Zc throughout the season
303 except for JJAS. During JJAS, a shallow Zc is seen near the coastal Arabian Sea (around 10 m to
304 35 m) presumably due to the coastal Chl-a blooms. Deep Zc off the coast of Sumatra (~ 40 m to
305 50 m) is found during JJAS. Java-Sumatra coastal upwelling is centered on September to

306 November (Susanto et al., 2001) and upwelling originates at around 100 m depth (Valsala and
307 Maksyutov, 2010; Xing et al., 2012).

308 Southward of 10°S in the oligotrophic gyre region, Z_c varies from 40 m to more than 60 m
309 throughout the year. A conspicuous feature observed while parameterizing the solar radiation
310 and Chl-a dependent Z_c is that its maximum value never crosses 75 m especially in the Indian
311 Ocean which is the value specified in OCMIP-II models. The cutoff depth of 75 m in OCMIP-II
312 is obtained from observing the seasonal variance in oxygen data (Najjar and Keeling, 1997) as an
313 indicator of the production zone. However, our results show that parameterizing a production
314 zone based on solar radiation and Chl-a predicts a production zone and its variability that is
315 largely less than 75 m. The relevance of $\text{var}Z_c$ in the seasonality of the modeled carbon cycle is
316 illustrated as follows.

317

318 **3.1. Simulated seasonal cycle of pCO_2 and CO_2 fluxes**

319 The annual mean biases in simulated CO_2 fluxes and pCO_2 were evaluated by comparing
320 with Takahashi et al., (2009) observations (Figure 4). The model biases are significantly reduced
321 with the implementation of $\text{var}Z_c$ compared to that of the constant Z_c (hereinafter $\text{const}Z_c$). A
322 notable reduction in pCO_2 bias (by $\sim 10\mu\text{atm}$) is observed along the WAS (Figure 4d).

323 In order to address the role of the new biological parameterization of a variable Z_c , we
324 have extended our study by choosing four key regions where the biological production and CO_2
325 fluxes are prominent in the Indian Ocean with additional sensitivity experiments (see
326 Introduction and references therein). The regions (boxes shown in Figure 1) we considered are,
327 (1) Western Arabian Sea (WAS; 40°E:65°E, 5°S:25°N) (2) Sri Lanka Dome (SLD; 81°E:90°E,

328 0°:10°N) (3) Seychelles-Chagos Thermocline Ridge (SCTR; 50°E:80°E, 5°S:10°S) and (4)
329 Sumatra Coast (SC; 90°E:110°E, 0°:10°S; Figure 1). The seasonal variations of Z_c over these
330 selected key regions are shown in Figure 5. A detailed analysis of CO_2 fluxes, pCO_2 , biological
331 export and new productions and the impact of var Z_c simulations in improving the strength of
332 biological pump and solubility pump for these key regions are presented below.

333

334 **3.2. Western Arabian Sea (WAS)**

335 The WAS Z_c has a double peak pattern over the annual cycle. During the February-March
336 period, Z_c deepens down to a maximum of 43.85 ± 2.3 m into March and then shoals to $25.75 \pm$
337 1.5 m (Figure 5) during the monsoon period (uncertainty represents the interannual standard
338 deviations of monthly data from 1990-2010). This shoaling of Z_c depth during the monsoon
339 indicates the potential ability of the present biological parameterization to capture the wind-
340 driven upwelling related production in the WAS. During the post-monsoon period, the second
341 deepening of Z_c occurs during November with a maximum depth of 34.91 ± 2.2 m. The ability to
342 represent the seasonality of the production zone renders a unique improvement in CO_2 flux
343 variability especially in the WAS in comparison to the OCMIP-II experiments (Orr et al, 2003;
344 Figure 6a).

345 OCMIP –II simulations with a const Z_c of 75 m underestimate the CO_2 flux when compared
346 to the observations of Takahashi et al. (2009). This underestimation is clearly visible during the
347 monsoon period. Our simulations with the var Z_c resulted in a better seasonality of CO_2 flux
348 when compared with Takahashi et al. (2009) observations (Figure 6a). The improvement due to
349 the var Z_c scheme is able to represent the seasonality of CO_2 flux better especially during the

350 monsoon period when wind-driven upwelling is dominant. Obviously, the relative role of the
351 biological and solubility pumps have to be deciphered in this context.

352 The CO₂ flux during July from observations, constZc, and varZc simulations are 3.09 mol m⁻²
353 yr⁻¹, 1.82 ± 0.4 mol m⁻² yr⁻¹ and 3.10 ± 0.5 mol m⁻² yr⁻¹, respectively. Southwesterly wind-driven
354 upwelling over the WAS especially off the Somali coast (Smith and Codispoti, 1980; Schott,
355 1983; Smith, 1984) and Oman (Bruce, 1974; Smith and Bottero, 1977; Swallow, 1984; Bauer et
356 al., 1991), pulls nutrient-rich subsurface waters closer to the surface while the available turbulent
357 energy due to the strong winds lead to mixed layer entrainment of the nutrients resulting in a
358 strong surface phytoplankton bloom (Krey and Babenerd, 1976; Banse, 1987; Bauer, 1991;
359 Brock et al, 1991). This regional bloom extends over 700 km offshore from the Omani coast due
360 to upward Ekman pumping driven by strong, positive wind-stress curl to the northwest of the low
361 level jet axis and the offshore advection (Bauer et al., 1991; Brock et al., 1991; Brock and
362 McClain, 1992a, b; Murtugudde and Busalacchi, 1999, Valsala, 2009) resulting in strong
363 outgassing of CO₂ flux and an enhanced pCO₂ in the WAS (Valsala and Maksyutov, 2013;
364 Sarma et al., 2002). The seasonal mean CO₂ flux during the southwest monsoon period (JJAS)
365 for constZc and varZc simulations are 1.44 ± 0.2 mol m⁻² yr⁻¹ and 2.31 ± 0.4 mol m⁻² yr⁻¹,
366 respectively. The biological parameterization of varZc considerably improves the average CO₂
367 flux during the monsoon period by 0.86 ± 0.1 mol m⁻² yr⁻¹. The annual mean CO₂ flux from
368 observations, constZc and varZc simulations are 0.94 mol m⁻² yr⁻¹, 0.80 ± 0.17 mol m⁻² yr⁻¹ and
369 1.07 ± 0.2 mol m⁻² yr⁻¹, respectively. The annual mean CO₂ flux is improved by 0.27 ± 0.05 mol
370 m⁻² yr⁻¹.

371 Seasonality in pCO₂ also shows a remarkable improvement during the southwest monsoon
372 period (Figure 6b). The pCO₂ with constZc is considerably lower at a value of 385.22 ± 3.5 µatm

373 during June compared to observational values of 392.83 μatm . However, varZc simulation
374 performs better in terms of pCO₂ variability. The peak value of pCO₂ reaches up to 405.42 \pm 5.8
375 μatm . The seasonal mean pCO₂ during the Southwest monsoon period from observations,
376 constZc, and varZc simulations are 397.58 μatm , 389.18 \pm 3.6 μatm and 399.95 \pm 5.0 μatm ,
377 respectively. The improvement in pCO₂ by varZc simulation is 10.76 \pm 1.3 μatm when compared
378 with the constZc simulation. This inherently infers that constZc simulation fails to capture the
379 pCO₂ driven by upwelling during the Southwest monsoon while the varZc simulation is
380 demonstrably better in representing this seasonal increase. The annual mean pCO₂ from
381 observations, constZc, and varZc simulations are 394.69 μatm , 389.62 \pm 3.9 μatm and 391.19 \pm
382 4.7 μatm , respectively. However, it is worth mentioning that there are parts of the year where the
383 constZc performs better compared to varZc. For instance, during MAM as well as in November,
384 the constZc simulation yielded a better comparison with the observed pCO₂ whereas varZc
385 simulation yields a reduced magnitude of pCO₂. This may well indicate the biological vs.
386 solubility pump controls on pCO₂ during the intermonsoons. The role of mesoscale variability in
387 the ocean dynamics may also play a role (Valsala and Murtugudde, 2015). Nevertheless, during
388 the most important season (JJAS) when the pCO₂, CO₂ fluxes, and biological production are
389 found to be dominant in the Arabian Sea, the varZc produces a better simulation.

390 The improvements shown by the use of varZc in the simulation of CO₂ flux and pCO₂ can be
391 elicited by further analysis of the model biological production. Figure 7 shows the comparison of
392 model export production and new production with observational export production from
393 satellite-derived NPP for constZc and varZc simulations. The model export production in the
394 constZc simulation is much weaker when compared to varZc simulation. The varZc simulation
395 has improved the model export production. Theoretically, the new and export productions in the

396 model should be in balance with each other (Eppley and Peterson, 1979). The constZc export
397 production is much weaker than new production and it is not in balance. In contrast, the varZc
398 simulation yields a close balance among them.

399 Compared with the observational export production which peaks in August at a value of
400 $154.78 \text{ g C m}^{-2} \text{ yr}^{-1}$, the varZc simulated export and new productions peak at a value of $160.44 \pm$
401 $20.4 \text{ g C m}^{-2} \text{ yr}^{-1}$ and $167.18 \pm 24.0 \text{ g C m}^{-2} \text{ yr}^{-1}$, respectively, but in July. A similar peak can be
402 observed in constZc simulated new production as well, with a value of $178.19 \pm 28.0 \text{ g C m}^{-2} \text{ yr}^{-1}$
403 ¹. This apparent shift of one month during JJAS in the model export production as well as in the
404 new production is noted as a caveat in the present set up which will need further investigation.
405 Arabian Sea production is not just limited by nutrients but also the dust inputs (Wiggert et al.,
406 2006). The dust-induced primary production in the WAS, especially over the Oman coast is
407 noted during August (Liao et al., 2016). The mesoscale variability in the circulation and its
408 impact on production and carbon cycle are also a limiting factor in this model as noted above.

409 The seasonal mean export production during the southwest monsoon period from satellite-
410 derived estimate is $123.57 \text{ g C m}^{-2} \text{ yr}^{-1}$, whereas for constZc and varZc simulations it is $84.81 \pm$
411 $16.0 \text{ g C m}^{-2} \text{ yr}^{-1}$ and $147.19 \pm 23.8 \text{ g C m}^{-2} \text{ yr}^{-1}$, respectively. The new biological
412 parameterization strengthens the model export production by $62.38 \pm 7.8 \text{ g C m}^{-2} \text{ yr}^{-1}$ for the
413 southwest monsoon period, which is over a 70% increase. This indicates a considerable impact
414 of the biological pump in the model simulated CO_2 flux and pCO_2 over the WAS. For constZc
415 simulation, the computed new production is slightly higher ($150.84 \pm 27.9 \text{ g C m}^{-2} \text{ yr}^{-1}$) than that
416 of varZc ($133.03 \pm 19.5 \text{ g C m}^{-2} \text{ yr}^{-1}$). The annual mean export production from observations,
417 constZc and varZc simulations are $94.31 \text{ g C m}^{-2} \text{ yr}^{-1}$, $77.41 \pm 15.1 \text{ g C m}^{-2} \text{ yr}^{-1}$ and 122.54 ± 25.2
418 $\text{g C m}^{-2} \text{ yr}^{-1}$, respectively.

419 To understand how the varZc parameterization strengthens the export production in the
420 model, we have analyzed the phosphate profiles. It appears that the varZc parameterization
421 allows more phosphate concentration (Figure 8a, b) in the production zone and thereby increases
422 the corresponding biological production (Figure 8c, d). The net export production in the model
423 during JJAS is consistent with the satellite data (Figure 7b). However, in the constZc case, the
424 exports are rather ‘flat’ throughout the season with the imperfect representation of seasonal
425 biological export. The Table 1-4 summarize all the values discussed here.

426 The impact of varZc in the biological and solubility pumps is computed as per Louanchi et
427 al., (1996, see Appendix A). The varZc parameterization has strengthened the biological as well
428 as the solubility pump in the model and thereby modifying the phosphate profiles and achieves a
429 seasonal balance in export versus new production (Figure 9a). During the monsoon period, the
430 varZc simulation increases the strength of the solubility and biological pumps by $10.43 \pm 1.3 \text{ g C}$
431 $\text{m}^{-2} \text{ yr}^{-1}$ and $106.52 \pm 9 \text{ g C m}^{-2} \text{ yr}^{-1}$, respectively (see Table 5 and 6). Similarly, the annual mean
432 strength of solubility pump and the biological pump is increased by $3.29 \pm 0.6 \text{ g C m}^{-2} \text{ yr}^{-1}$ and
433 $81.18 \pm 9.92 \text{ g C m}^{-2} \text{ yr}^{-1}$, respectively. This supports the fact that the varZc parameterization
434 basically modifies the biological and solubility pumps in the model simulation and thereby
435 improves the seasonal cycle of CO₂ flux and pCO₂.

436

437 **3.3 Sri Lanka Dome (SLD)**

438 The seasonal variation in Zc for SLD has a similar pattern as that of WAS. Zc deepens to its
439 maximum during March up to $45.23 \pm 0.3 \text{ m}$ and reaches its minimum during the following
440 monsoon period at $30.79 \pm 1.5 \text{ m}$ (Figure 5). The similarities of varZc between WAS and SLD

441 indicates that they both are under similar cycles of solar influx and biological production. The
442 SLD Chl-a dominates only up to July (Vinayachandran et al., 2004) which explains why
443 production with varZc increases earlier compared to WAS which occurs during August-October.

444 The seasonality in CO₂ flux and pCO₂ were compared with Takahashi et al., (2009)
445 observations (Figure 10). varZc results in a slight improvement in CO₂ flux when compared with
446 constZc (Figure 10a). However, both constZc and varZc simulations underestimate the
447 magnitude of CO₂ flux when compared with observations. The seasonal mean CO₂ flux during
448 the monsoon period is 1.79 mol m⁻² yr⁻¹ from observations, which means SLD region is a source
449 of CO₂. But the mean values of constZc and varZc simulations yield flux values of -0.008 ± 0.2
450 mol m⁻² yr⁻¹ and 0.24 ± 0.2 mol m⁻² yr⁻¹, respectively. The constZc simulation misrepresents the
451 SLD region as a sink of CO₂ during monsoon period which is opposite to that of observations.
452 The varZc simulation corrects this misrepresentation to a source albeit at a smaller magnitude by
453 0.24 ± 0.09 mol m⁻² yr⁻¹ for the monsoon period. Compared to observations, the varZc case
454 underestimates the magnitude of JJAS mean by 1.55 mol m⁻² yr⁻¹.

455 The annual mean CO₂ fluxes for constZc and varZc simulations are -0.02 ± 0.1 mol m⁻² yr⁻¹
456 and 0.10 ± 0.2 mol m⁻² yr⁻¹, respectively. The varZc parameterization leads to an improvement of
457 0.13 ± 0.1 mol m⁻² yr⁻¹ in the annual mean CO₂ flux when compared with constZc simulation.
458 The observational annual mean of CO₂ flux is 0.80 mol m⁻² yr⁻¹ which is highly underestimated
459 by both simulations. This indicates a regulation of biological production of the region by varZc
460 which makes this region a source of CO₂ during monsoon. The role of the solubility pump may
461 also be underestimated due to the biases in the physical drivers and the lack of mesoscale eddy
462 activities in these simulations (Prasanna Kumar et al., 2002; Valsala and Murtugudde, 2015).

463 The seasonality of pCO₂ (Figure 10b) especially in the monsoon period is significantly
464 improved. The mean pCO₂ during the monsoon season from observation over the SLD region is
465 382.44 μatm. The seasonal mean pCO₂ during monsoon period for constZc and varZc
466 simulations are 371.67 ± 6.04 μatm and 379.24 ± 8.9 μatm, respectively. The annual mean pCO₂
467 from observations, constZc, and varZc simulations are 380.21 μatm, 370.76 ± 6.1 μatm and
468 374.94 ± 9.6 μatm, respectively. varZc simulations improve the JJAS mean pCO₂ by 7.56 ± 2.8
469 μatm and the annual mean pCO₂ by 4.18 ± 3.5 μatm, which is reflected in CO₂ flux as well. This
470 is likely due to the impact of new biological parameterization in capturing the episodic upwelling
471 in the SLD region which is further investigated by looking at its biological production.

472 The SLD biological production is highly exaggerated by the model for both constZc and
473 varZc simulations (Figure 11a, b). The seasonal mean biological export for the monsoon period
474 is 51.54 g C m⁻² yr⁻¹ as per satellite-derived estimates. However, the constZc and varZc
475 simulations overestimate it at 167.71 ± 59.04 g C m⁻² yr⁻¹ and 151.51 ± 46.4 g C m⁻² yr⁻¹,
476 respectively. This exaggerated export is visible in climatological annual means where for
477 constZc and varZc simulations they are 144.43 ± 49.8 g C m⁻² yr⁻¹ and 156.08 ± 43.8 g C m⁻² yr⁻¹,
478 respectively.

479 For constZc simulation, new production is overestimated from March to October when
480 compared to observations and the second peak is observed in November (Figure 11a). But the
481 overestimate in new production with varZc is observed only during JJAS period by a value of
482 26.23 g C m⁻² yr⁻¹. For the SLD region, the varZc parameterization overestimates the export
483 production but minimizes the excess new production, especially in the monsoon period by 64.15
484 ± 36.4 g C m⁻² yr⁻¹. This indicates that the varZc parameterization is somewhat successful in

485 capturing the upwelling episode during the monsoon over SLD. All values are summarized in
486 Table 1 to 4.

487 The solubility and biological pumps are modified by the varZc parameterization significantly
488 when compared with the constZc simulation (Figure 9b). Over the monsoon period, the strength
489 of the solubility and biological pumps are improved by $2.81 \pm 1.1 \text{ g C m}^{-2} \text{ yr}^{-1}$ and $66.68 \pm 9.7 \text{ g}$
490 $\text{C m}^{-2} \text{ yr}^{-1}$, respectively. Similarly, the annual mean strength of solubility and biological pump
491 are increased by $0.99 \pm 1.2 \text{ g C m}^{-2} \text{ yr}^{-1}$ and $52.5 \pm 5.1 \text{ g C m}^{-2} \text{ yr}^{-1}$ respectively. All values are
492 provided in Table 5 and 6.

493

494 **3.4 Sumatra Coast (SC)**

495 The seasonal variation in Zc over the SC region lies between 40 m and 46 m (Figure 5). The
496 seasonal maximum occurs during January to March, especially in March with a depth of 45.5 m.
497 During the monsoon period, Zc shoals slightly with a minimum of 41.1 m in July. The variation
498 in Zc is relatively small as compared to the other regions which is consistent with its relatively
499 low production throughout the year.

500 The seasonality of CO₂ flux and pCO₂ captured by constZc and varZc simulations are shown
501 in Figure 12a, b. The varZc simulations overestimate both CO₂ flux and pCO₂, especially during
502 the monsoon. It is found that the constZc simulation is better compared to varZc simulation. The
503 varZc simulation overestimates the seasonal mean CO₂ flux and pCO₂ by $1.19 \text{ mol m}^{-2} \text{ yr}^{-1}$ and
504 $29.61 \text{ } \mu\text{atm}$, respectively, compared to observations (Table 1). However, constZc produces a
505 better estimate compared with observations for CO₂ flux and pCO₂. The constZc simulation
506 delivers a better annual mean than varZc (Table 1, 2). The annual mean bias in constZc and

507 varZc simulations for CO₂ flux is -0.0033 mol m⁻² yr⁻¹ and 0.31 mol m⁻² yr⁻¹, respectively.
508 Similarly, pCO₂ bias is 1.95 μatm and 9.07 μatm for constZc and varZc simulations.

509 Biological production simulated by the model along SC explains the overestimation of CO₂
510 flux and pCO₂ (Figure 13). Both constZc and varZc simulations greatly overestimate export
511 production in the model. However, a small enhancement in the new production during JJAS in
512 constZc case is an indicator of upwelling episodes. The seasonal mean new production during
513 the monsoon from constZc and varZc are 63.64 ± 30.9 g C m⁻² yr⁻¹ and 78.11 ± 29.1 g C m⁻² yr⁻¹,
514 respectively (Table 4). The seasonal mean export production during the monsoon from
515 observations is 58.87 g C m⁻² yr⁻¹ (Table 3). The constZc simulation represents a better new
516 production, which is seen as a relatively small exaggeration of CO₂ flux and pCO₂. The
517 biological response of SC is found to be better with constZc which is in contradiction to a
518 general improvement found with varZc in the other regions examined here. Such discrepancies
519 over the SC could be due to the effect of Indonesian Throughflow (Bates et al., 2006) which is
520 not completely resolved in the model due to coarse spatial resolution (also see Valsala et al.,
521 2010).

522 The overestimation of export production by varZc simulation is also evident by the increase
523 in strength of the biological and solubility pumps, respectively (Figure 9c). The annual mean and
524 JJAS mean DIC increases in the production zone due to the biological pump is 67.21 ± 1.3 g C
525 m⁻² yr⁻¹ and 83.62 ± 0.5 g C m⁻² yr⁻¹, respectively. Similarly the increase in DIC due to the effect
526 of solubility pump during the JJAS period and annual mean are 10.95 ± 5.2 g C m⁻² yr⁻¹ and 3.87
527 ± 2.2 g C m⁻² yr⁻¹ respectively (see table 5 and 6).

528

529 3.5 Seychelles-Chagos Thermocline Ridge (SCTR)

530 The SCTR is a unique open-ocean upwelling region with a prominent variability in air-sea
531 interactions (Xie et al., 2002). Wind-driven mixing and upwelling of subsurface nutrient-rich
532 water play a major role in the biological production of this region (Dilmahamod et al., 2016).
533 The seasonal cycle in Z_c is shown in Figure 5. The maximum Z_c occurs in November at about
534 44.94 m and the minimum at 33.2 m in July. The shoaling of Z_c during the monsoon period
535 shows that the biological parameterization captures the upwelling response over this region.

536 The seasonality of CO_2 flux and pCO_2 are shown in Figure 14. The Takahashi observations
537 of CO_2 flux shows a peak in June with outgassing of CO_2 during the upwelling episodes.
538 However, both constZc and varZc simulations underestimate this variability. The seasonality of
539 CO_2 flux in varZc shows a significant improvement when compared to constZc simulation, but
540 underestimated when compared to observations. The seasonal mean CO_2 flux during the
541 monsoon from observations, constZc and varZc simulations are $0.82 \text{ mol m}^{-2} \text{ yr}^{-1}$, -0.32 ± 0.3
542 $\text{mol m}^{-2} \text{ yr}^{-1}$ and $-0.05 \pm 0.4 \text{ mol m}^{-2} \text{ yr}^{-1}$, respectively. This represents a reduction in the seasonal
543 mean sink of CO_2 flux in the SCTR region during the monsoon by $0.27 \pm 0.1 \text{ mol m}^{-2} \text{ yr}^{-1}$
544 bringing it closer to a source region (see Table 1 for details).

545 The improved CO_2 flux is also supported by the seasonal cycle in pCO_2 . Based on
546 observations, the seasonal mean of pCO_2 with constZc during JJAS is underestimated by 11.47
547 μatm , varZc simulation underestimates it by 6.45 μatm . So it is evident that varZc simulation
548 capture the upwelling episodes better, marked by a larger pCO_2 during JJAS period. However,
549 the magnitude of pCO_2 is still underestimated compared to observations (Table 2).

550 Figure 15 shows the biological production of constZc and varZc simulations for SCTR. It is
551 clear that both simulations overestimate the export production and underestimate the new
552 production. The JJAS mean export production from observations, constZc and varZc are 51.08 g
553 C m⁻² yr⁻¹, 57.39 ± 14.2 g C m⁻² yr⁻¹ and 99.23 ± 29.8 g C m⁻² yr⁻¹, respectively. The varZc
554 simulations exaggerate the model export production by 48.14 g C m⁻² yr⁻¹. The varZc simulation
555 improves the JJAS mean new production by 1.14 ± 2.2 g C m⁻² yr⁻¹ (Table 4). The DIC variations
556 due to the biological pump over the monsoon period and the annual mean also support the
557 exaggerated export production. During the monsoon period, the varZc simulation strengthens the
558 biological and solubility pump by 72.64 ± 6.2 g C m⁻² yr⁻¹ and -4.56 ± 1.6 g C m⁻² yr⁻¹,
559 respectively when compared to the constZc simulation (Figure 9d). This is also reflected in the
560 annual mean DIC variations due to the biological and solubility pump effects (see table 5 and 6).
561 This slight improvement in the model new production, especially during the monsoon period
562 signals that the varZc better captures the upwelling over SCTR. Considering the annual mean
563 values of model export and new production, constZc simulation is reasonably faithful to
564 observations.

565 The underestimation of CO₂ and pCO₂, as well as the exaggeration of model export
566 production and a slight, overestimate in model new production may be due to two reasons; (1)
567 SCTR is a strongly coupled region with remote forcing of the mixed layer – thermocline
568 interactions (Zhou et al., 2008) which can affect the seasonality in biological production that the
569 model may not be resolving reasonably, (2) the bias associated with physical drivers, especially
570 wind stress may underestimate the CO₂ flux as well biological production. A similar
571 overestimation of biological production was also reported in a coupled biophysical model
572 (Dilmahamod et al., 2016).

573 Table 1 – 4 shows the entire summary of seasonal and annual mean CO₂ flux, pCO₂ and
574 biological production reported in Section 3.

575

576 **4. Sensitivity Simulations**

577 From the analysis of four major upwelling regions over the Indian Ocean, it is evident that
578 the biological parameterization of varZc better captures upwelling episodes and thus it enhances
579 the model export production. This is most clearly visible over the WAS region. In order to
580 quantify how much the varZc parameterization contributes to the seasonality of carbon cycle,
581 two additional sensitivity simulations are carried out; viz. (1) with annual mean offline currents
582 and (2) annual mean offline temperatures with the goal of suppressing the dynamical and
583 thermodynamical effects of seasonal upwelling over WAS (see Section 2 for details). The focus
584 on this region is motivated by its prominence as the most productive zone of the Indian Ocean.
585 Moreover, the improvement in the biological processes in the model by the varZc
586 parameterization is best captured in this region. The results are discussed below.

587

588 **4.1 Impact of varZc parameterization on seasonality of carbon cycle with annual** 589 **mean currents.**

590 To quantify the impact of varZc parameterization, the model is forced with annual mean
591 currents only over WAS region with unaltered currents in the rest of the ocean. The hypothesis is
592 that the muting of the seasonal variability of Ekman divergence removes the upwelling and the
593 biological pump contribution to production and carbon cycle. The comparison of constZc and

594 varZc then allows us to decipher the impact of varZc in capturing the impacts of upwelling on
595 biological production and the carbon cycle. The smooth blending of currents at the boundary of
596 the WAS domain is achieved by a linear smoothing function as given in Section 2.

597 The model biological responses (inferred by comparing with the control run) in terms of the
598 CO₂ flux shows a flat pattern over the monsoon period for constZc simulation (Figure 16a).
599 While the varZc simulation forced with the annual mean currents shows an enhanced CO₂ flux
600 indicating the outgassing of CO₂ flux over WAS due to wind-driven upwelling (Figure 16b).
601 This qualitatively shows that the varZc itself has improved the seasonality in the biological
602 processes (export and new production) and captured the upwelling episodes during the monsoon.
603 The varZc parameterization is responsible for an improvement of $0.48 \pm 0.04 \text{ mol m}^{-2} \text{ yr}^{-1}$ and
604 $0.13 \pm 0.02 \text{ mol m}^{-2} \text{ yr}^{-1}$ in the JJAS seasonal and annual mean CO₂ fluxes, respectively. This
605 improves the overall model CO₂ flux in the control run especially in July (Figure 16b).

606 Similar improvements are also noticed in pCO₂ (Figure 17). In the constZc simulation
607 with annual mean currents, the pCO₂ dips down during JJAS monsoon period which indicates
608 the inadequacy of constZc in capturing the upwelling enriched pCO₂ difference (Figure 17a, b).
609 The varZc simulation slightly modifies the pCO₂ in the ‘right’ direction during JJAS despite the
610 annual mean currents.

611 The export and new productions in the model explain the modification of CO₂ flux and
612 pCO₂ by varZc parameterization. The biological export production is highly underestimated in
613 the constZc simulation forced with annual mean currents while the varZc simulation captures the
614 seasonal upswing in production (Figure 18). The improved JJAS mean and annual mean export
615 production by $43.51 \pm 8.6 \text{ g C m}^{-2} \text{ yr}^{-1}$ and $30.28 \pm 13.7 \text{ g C m}^{-2} \text{ yr}^{-1}$, respectively is a clear

616 indication of the positive impacts of a varZc. Similarly, the improvement in JJAS mean and
617 annual mean new production (Figure 19) from varZc simulated with annual mean currents are
618 $17.39 \pm 0.8 \text{ g C m}^{-2} \text{ yr}^{-1}$ and $14.81 \pm 0.1 \text{ g C m}^{-2} \text{ yr}^{-1}$, respectively. In short the varZc biological
619 parameterization improves the export and new productions in the model. This helps the model to
620 capture the upwelling episodes over the study regions. Table 7 summarizes all the results of
621 biological sensitivity runs.

622

623 **4.2 Impact of varZc parameterization on seasonality of carbon cycle with annual** 624 **mean temperatures.**

625 By imposing the annual mean temperature over WAS region, we are suppressing the cooling
626 effect of temperature due to upwelling and quantifying how much the model seasonality is
627 improved due to varZc parameterization. (see Section 2 for details). The varZc simulations
628 forced with annual mean SST has larger JJAS mean and annual mean CO₂ fluxes by 0.88 ± 0.1
629 $\text{mol m}^{-2} \text{ yr}^{-1}$ and $0.28 \pm 0.07 \text{ mol m}^{-2} \text{ yr}^{-1}$, respectively (Figure 20 and Table 8). For a given
630 annual mean SST the solubility pump largely controls the CO₂ emission during JJAS if a varZc
631 is prescribed, likely by the enrichment of DIC (inferred from Figure 8b). Similarly, the
632 improvement in pCO₂ (Figure 21) with varZc simulation is also remarkable. The JJAS mean and
633 annual mean improvements from the implementation of varZc are $11.05 \pm 1.9 \text{ } \mu\text{atm}$ and $1.91 \pm$
634 $1.4 \text{ } \mu\text{atm}$, respectively. The detailed quantification of CO₂ and pCO₂ responses for this
635 experimental setup is given in Table 8. The above analysis adds supporting evidence that the
636 varZc simulation strengthens the seasonality of the model compared to the constZc case. This is

637 presumably accomplished by the more accurate Z_c and production zone implied with a variable
638 Z_c .

639

640 **5. Summary and Conclusions**

641 A spatially and temporally varying Z_c parameterization as a function of solar radiation and
642 Chl-a is implemented in the biological pump model of OCMIP-II for a detailed analysis of
643 biological fluxes in the upwelling zones of the Indian Ocean. The var Z_c parameterization
644 improves the seasonality of model CO_2 flux and pCO_2 variability, especially during the monsoon
645 period. A significant improvement is observed in WAS where the monsoon wind-driven
646 upwelling dominates biological production. The magnitude of CO_2 flux matches with
647 observations, especially in July when monsoon winds are at their peak. Monsoon triggers
648 upwelling in SLD as well which acts as a source of CO_2 to the atmosphere. The seasonal and
649 annual mean are underestimated with const Z_c and the SLD is reduced to a sink of CO_2 flux. The
650 var Z_c simulation modifies the seasonal and annual means of the CO_2 flux of SLD and depict it as
651 a source of CO_2 especially during the monsoon, but the magnitude is still underestimated
652 compared to Takahashi et al. (2009) observations. The SCTR variability is underestimated by
653 both const Z_c and var Z_c simulations, portraying it as a CO_2 sink region whereas observations
654 over the monsoon period indicate that the thermocline ridge driven by the open ocean wind-
655 stress curl is, in fact, an oceanic source of CO_2 . However, the var Z_c simulation reduces the
656 magnitude of the sink in this region bringing it relatively close to observations.

657 Var Z_c biological parameterization strengthens the export and new productions in the model,
658 which allows it to represent a better seasonal cycle of CO_2 flux and pCO_2 over the study regions.

659 The WAS export production is remarkably improved by $62.37 \pm 7.8 \text{ g C m}^{-2} \text{ yr}^{-1}$ compared to
660 constZc. This supports our conclusion that the varZc parameterization increases the strength of
661 biological export in the model. Over the SLD, the JJAS seasonal mean export and new
662 production are underestimated in varZc compared to constZc simulations, but the annual mean
663 export production is improved. Export production at SC and SCTR are highly exaggerated and
664 there is hardly any improvement in new production with a variable Zc especially over the
665 monsoon period. The inability of varZc parameterization to improve the seasonality of SC and
666 SCTR may be due to the interannual variability of biological production associated with the
667 Indonesian throughflow and remote forcing of the mixed layer-thermocline interactions and the
668 effect of biases in the wind stress data used as a physical driver in the model.

669 Sensitivity experiments carried out by prescribing annual mean currents or temperatures over
670 selected subdomains reveal that the varZc retains the seasonality of carbon fluxes, pCO₂, and
671 export and new productions closer to observations. This strongly supports our contention that
672 varZc parameterization improves export and new productions and it is also efficient in capturing
673 upwelling episodes of the study regions. This points out the significant role of having a close
674 balance in seasonal biological export and new production in models to capture the seasonality in
675 the carbon cycle. This also confirms the role of biological and solubility pumps in producing the
676 seasonality of carbon cycle in the upwelling zones.

677 However, the underestimation of the seasonality of CO₂ flux over the SLD and
678 overestimation over the SC as well as the SCTR are a cautionary flag for the study. This
679 uncertainty poses an important scientific question as to whether the model biology over the SC
680 and SCTR region is not resolving the seasonality in CO₂ flux and pCO₂ properly or whether the
681 seasonality in the Zc is not able to fully capture the biological processes.

682 To address these questions we have used an inverse modeling approach (Bayesian inversion)
683 in order to optimize the spatially and temporally varying Z_c using surface pCO_2 as the
684 observational constraint and computed the optimized biological production. The results will be
685 reported elsewhere.

686

687

688

689

690

691

692

693

694

695

696

697

698

699

700 **Appendix – A**

701 The time evolution equations of the model variables are given by

$$702 \quad \frac{d[PO_4]}{dt} = L([PO_4]) + J_b PO_4 \quad (A1)$$

$$703 \quad \frac{d[DOP]}{dt} = L([DOP]) + J_b DOP \quad (A2)$$

$$704 \quad \frac{dDIC}{dt} = L([DIC]) + J_b DIC + J_g DIC + J_v DIC \quad (A3)$$

$$705 \quad \frac{d[ALK]}{dt} = L([ALK]) + J_b ALK + J_v ALK \quad (A4)$$

706 Where L is the 3D transport operator, which represents the effects of advection, diffusion, and
 707 convection. [] or square brackets indicate the concentrations in mol m⁻³. $J_b PO_4$, $J_b DOP$, $J_b DIC$,
 708 $J_b ALK$ is the biological source/sink terms and $J_v DIC$, $J_v ALK$ are the virtual source-sink terms
 709 representing the changes in surface DIC and ALK, respectively, due to evaporation and
 710 precipitation. $J_v DIC$ is the source-sink term due to air-sea exchange of CO₂.

711 The following equations represent for the biological processes in the model

712 For $Z < Z_c$,

$$713 \quad J_{prod} = \frac{1}{\tau} ([PO_4] - [PO_4^*]), \quad [PO_4] > [PO_4^*] \quad (A5)$$

$$714 \quad J_{DOP} = \sigma J_{prod} - \kappa [DOP] \quad (A6)$$

$$715 \quad J_{PO_4} = -J_{prod} + \kappa [DOP] \quad (A7)$$

$$716 \quad J_{ca} = Rr_{C:P} (1 - \sigma) J_{prod} \quad (A8)$$

$$717 \quad J_{DIC} = r_{C:P}J_{PO4} + J_{ca} \quad (A9)$$

$$718 \quad J_{ALK} = -r_{N:P}J_{PO4} + 2J_{ca} \quad (A10)$$

719 For $Z > Z_c$,

$$720 \quad J_{prod} = 0, \quad [PO_4] \leq [PO_4^*] \quad (A11)$$

$$721 \quad J_{DOP} = -\kappa[DOP] \quad (A12)$$

$$722 \quad J_{PO4} = -\frac{\partial F}{\partial Z} + \kappa[DOP] \quad (A13)$$

$$723 \quad F_c = (1 - \sigma) \int_0^{Z_c} J_{prod} dZ \quad (A14)$$

$$724 \quad F(Z) = F_c \left(\frac{Z}{Z_c}\right)^a \quad (A15)$$

$$725 \quad J_{ca} = -\frac{\partial F_{ca}}{\partial Z} \quad (A16)$$

$$726 \quad F_{ca} = R r_{C:P} F_c e^{-(Z-Z_c)/d} \quad (A17)$$

727 Where Z is the depth and Z_c is the compensation depth in the model. J_{DOP} and J_{PO4} are the
728 biogeochemical sources and sinks and J_{prod} , J_{ca} represents the biogeochemical flows with
729 respect to production and calcification. Within Z_c , the production of organic phosphorous in the
730 model J_{prod} is calculated using equation A5. $[PO_4]$ is the model phosphate concentration and
731 $[PO_4^*]$ is observational phosphate. τ is the restoration timescale assumed to be 30 days. Whenever
732 the model phosphate exceeds the observational phosphate, it allows production, below which the
733 production is zero. The observational phosphate data were taken from the World Ocean Atlas
734 (WOA; Garcia et al., 2014). It is assumed that a fixed fraction (σJ_{prod}) of phosphate uptake is

735 converted into Dissolved Organic Phosphorus (DOP) which is a source for J_{DOP} (equation A6).
736 The phosphate not converted to DOP results in an instantaneous downward flux of particulate
737 organic phosphorus at Z_c (equation A14). The decrease of flux with depth due to
738 remineralization is shown by a power law relationship as in equation A15. The values of the
739 constants a , κ , σ are 0.9, 0.2/year to 0.7/year, 0.67, respectively. The rate of production is used to
740 explain the formation of calcium carbonate cycle in surface waters (equation A8) and its export
741 is given by equation A16, where R is the rain ratio, a constant molar ratio of exported particulate
742 organic carbon to the exported calcium carbonate flux at Z_c . The exponential decrease of
743 calcium carbonate flux with scale depth d is given by equation A17. The biological source or
744 sink of dissolved inorganic carbon (DIC) and alkalinity (ALK) is explained through equations
745 A9 and A10, respectively. Where the values of rain ratio (R) is taken as 0.07 and the Redfield
746 ratio, $r_{C:P} = 117$, and $r_{N:P} = 16$ and scale depth d is chosen as 3500m.

747

748 **Biological and Solubility Pump calculations**

749 The biological effect on DIC is calculated from Louanchi et al., (1996). The tendency of DIC
750 due to biomass production and calcite formation in the production zone is expressed as below.

$$751 \quad \left(\frac{\partial DIC}{\partial t}\right)_b = \left(\frac{\partial PO_4}{\partial t}\right)_b \times R_{C:P} - J_{Ca} \quad (A18)$$

752 The total tendency of DIC in the production zone is:

$$753 \quad \left(\frac{\partial DIC}{\partial t}\right)_{total} = \left(\frac{\partial DIC}{\partial t}\right)_b + \int_x \int_y F dx dy \quad (A19)$$

754 where $\left(\frac{\partial DIC}{\partial t}\right)_b$ is the evolution of DIC due to the impact of biology (i.e., biological pump). The
755 first term in the R.H.S of Equation A18 is the rate of change of phosphate resulting from
756 photosynthesis and respiration in the model (i.e., J_{po4} in this case) multiplied by the carbon to
757 phosphorous Redfield ratio ($R_{C:P} = 117:1$) and J_{Ca} represents the calcite formation in the model
758 (see Equation A8 & A16). The solubility pump is calculated as the surface integral of the flux F
759 (Louanchi et al., 1996).

760

761 **Appendix B**

762 In order to compare our model production of organic phosphorous to the curve of Ryther et al.,
763 (1956) we have merely scaled our total production to “relative photosynthesis”, which is,
764 according to Ryther et al., (1956) is an index between 0 and 1 indicating the strength of
765 production estimated as P_l/P_{max} . Here P_l is the photosynthesis at each intensity (of light) of
766 different species and P_{max} is the maximum photosynthesis observed in the same control
767 experiment. The curve between relative photosynthesis and light intensity shows the relation
768 between photosynthetic activity and light in marine phytoplankton. Since our method relates
769 biological production to a function of light (limitation) by Chl-a attenuation, it is the best curve
770 to cross-compare our results. In this case we scaled our total biological production within Z_c into
771 relative values between 0-1 by P_l/P_{max} . in which P_l is taken as the individual grid cell biological
772 component of organic phosphorus production and P_{max} is the maximum production available in
773 the domain at any given instant. All the grid points are quite similar to the curve of Ryther et al.,
774 (1956) as shown in Figure 2.

775

776 **Acknowledgements**

777 Thanks to two anonymous reviewers and the editor (Marilaure Grégoire) for comments. Sreeush
778 M. G. sincerely acknowledges the fellowship support from Indian Institute of Tropical
779 Meteorology (IITM) to carry out the study. The OCMIP-II routines were taken from
780 (<http://ocmip5.ipsl.jussieu.fr/OCMIP/>). GFDL data for OTTM is taken from
781 (<http://data1.gfdl.noaa.gov/nomads/forms/assimilation.html>). Takahashi data is taken from
782 (<http://www.ldeo.columbia.edu/res/pi/CO2/>) and SeaWiFS data is obtained from the National
783 Aeronautics and Space Administration (NASA) Ocean Color Website
784 (<http://oceancolor.gsfc.nasa.gov/>). The computations were carried out in High-Performance
785 Computing (HPC) facility of Ministry of Earth Sciences (MoES), IITM.

786

787

788

789

790

791

792

793

794

795 **References**

796 Anderson, L. A., Sarmiento, J. L.: Global ocean phosphate and oxygen simulations, *Global*
797 *Biogeochem. Cycles*, 9, 621-636, doi:10.1029/95GB01902, 1995.

798 Asselin, R.: Frequency filter for time integrations, *Mon. Wea. Rev.*, 100, 487–490, doi:
799 10.1175/1520-0493, 1972.

800 Banse, K., McClain, C. R.: Winter blooms of phytoplankton in the Arabian Sea as observed by
801 the Coastal Zone Color Scanner, *Mar. Ecol. Prog. Ser.*, 34, 201 – 211, 1986.

802 Banse, K.: Seasonality of phytoplankton chlorophyll in the central and northern Arabian Sea,
803 *Deep Sea Res.*, 34, 713 – 723, doi:10.1016/0198-0149, 1987.

804 Barber, R. T., Marra, J., Bidigare, R. C., Codispoti, L. A., Halpern, D., Johnson, Z., Latasa, M.,
805 Goericke, R., and Smith, S. L.: Primary productivity and its regulation in the Arabian Sea during
806 1995, *Deep. Sea. Res. pt. II*, 48, 1127 – 1172. doi:10.1016/S0967-0645, 2001.

807 Bates, N. R., Pequignet, A. C., and Sabine, C. L.: Ocean carbon cycling in the Indian Ocean: 2.
808 Estimates of net community production, *Global Biogeochem. Cycles.*, 20, GB3021,
809 doi:10.1029/2005GB002492, 2006.

810 Bauer, S., Hitchcock, G. L., Olson, D. B.: Influence of monsoonally-forced Ekman dynamics
811 upon surface-layer depth and plankton biomass distribution in the Arabian Sea, *Deep Sea Res.*,
812 38, 531 – 553, doi:10.1016/0198-0149, 1991.

813 Behrenfeld, M. J., Falkowski, P. G.: Photosynthetic rates derived from satellite-based
814 chlorophyll concentration, *Limnol. Oceanogr.*, 42, 1 – 20, doi: 10.4319/lo.1997.42.1.0001, 1997.

815 Boyd, P. W., Rynearson, T. A., Armstrong, E. A., Fu, F., Hayashi, K. and co-authors.: Marine
816 Phytoplankton Temperature versus growth responses from polar to tropical waters – outcome of
817 a scientific community-wide study, PLoS ONE 8(5), e63091,
818 Doi:10.1371/journal.pone.0063091, 2013.

819 Brock, J. C., McClain, C. R.: Interannual variability of the southwest monsoon phytoplankton
820 bloom in the north-western Arabian Sea, J. Geophys. Res., 97(C1), 733 – 750,
821 doi/10.1029/91JC02225, 1992.

822 Brock, J. C., McClain, C. R., Hay, W. W.: A southwest monsoon hydrographic climatology for
823 the northwestern Arabian Sea, J. geophys. Res., 97(C6), 9455 – 9465, doi: 10.1029/92JC00813,
824 1992.

825 Brock, J. C., McClain, C. R., Luther, M. E., Hay, W. W.: The phytoplankton bloom in the
826 northwestern Arabian Sea during the southwest monsoon of 1979, J. Geophys. Res., 96(C11),
827 623 – 642, doi: 10.1029/91JC01711, 1991.

828 Brock, J., Sathyendranath, S., and Platt, T.: Modelling the seasonality of subsurface light and
829 primary production in the Arabian Sea, Mar. Eco. Prog. Ser., 101, 209 – 221, 1993.

830 Bruce, J. G.: Some details of upwelling off the Somali and Arabian coasts, J. Mar. Res., 32, 419
831 – 423, 1974.

832 Bryan, K., Lewis, L. J.: A water mass model of the world ocean, J. Geophys. Res., 84, 2503 –
833 2517, doi: 10.1029/JC084iC05p02503, 1979.

834 Chang, Y. S., Zhang. S., Rosati. A., Delworth. T., Stern. W. F.: An assessment of oceanic
835 variability for 1960-2010 from the GFDL ensemble coupled data assimilation, *Clim. Dyn.*, 40,
836 775 – 803, doi: 10.1007/s00382-012-1412-2, 2012.

837 Christian J. R., Verschall M. A., Murtugudde R., Busalacchi A. J., McClain C. R.:
838 Biogeochemical modeling of the tropical Pacific Ocean. II: Iron biogeochemistry, *Deep Sea*
839 *Res.*, 49, 545 – 565, doi:10.1016/S0967-0645, 2001.

840 Colwell, R. R.: Global climate and infectious disease: the cholera paradigm, *Science.*, 274(5295),
841 2025 – 2031, doi: 10.1126/science.274.5295.2025, 1996.

842 Dickson, A. G., and F. J. Millero.: A comparison of the equilibrium constants for the dissociation
843 of carbonic acid in seawater media, *Deep-Sea Res.*, 34, 1733 – 1743, 1987.

844 Dilmahamod A. F., Hermes. J. C., Reason C. J. C.: Chlorophyll-a variability in the Seychelles-
845 Chagos Thermocline Ridge: Analysis of a coupled biophysical model, *J. of. Mar. Sys.*, 154, 220
846 – 232, doi:10.1016/j.jmarsys.2015.10.011, 2016.

847 Doney S. C., and co-authors.: Evaluating global ocean carbon models: The importance of
848 realistic physics, *Glob. Biogeochem. Cycles*, 18, doi:10.1029/2003GB002150, 2004.

849 Eppley, R. W., Peterson. B. J.: Particulate organic matter flux and planktonic new production in
850 the deep ocean, *Nature*, 282, 677-680, doi:10.1038/282677a0, 1979.

851 Eppley, R. W.: Temperature and phytoplankton growth in the sea, *Fish. Bull.*, 70, 1063 – 1085,
852 1972.

853 Falkowski, P. G., E. A. Laws, R. T. Barber, and J. W. Murray: phytoplankton and their role in
854 the primary, new and export production, In: Fasham M.J.R (eds) *Ocean Biogeochemistry*, Global

855 Change – The IGBP series (closed). Springer, Berlin, Heidelberg, doi:
856 https://doi.org/10.1007/978-3-642-55844-3_5, 2003.

857 Feely, R. A., Sabine, C. L., Takahashi, T., Wanninkhof, R.: Uptake and Storage of Carbon
858 Dioxide in the Ocean: The Global CO₂ Survey, *Oceanography.*, 14(4), 18–32,
859 doi:10.5670/oceanog.2001.03, 2001.

860 Friedrichs, M. A. M., and co-authors.: Assessment of skill and portability in regional
861 biogeochemical models: role of multiple planktonic groups, *J. Geophys. Res.*, 112, doi:
862 10.1029/2006JC003852, 2007.

863 Friedrichs, M. A. M., Hood, R. R., Wiggert, J. D.: Ecosystem complexity versus physical forcing
864 quantification of their relative impact with assimilated Arabian Sea data, *Deep Sea Res.*, 53, 576-
865 600, doi:10.1016/j.dsr2.2006.01.026, 2006.

866 Garcia, H. E., R. A. Locarnini, T. P. Boyer, J. I. Antonov, O.K. Baranova, M.M. Zweng, J.R.
867 Reagan, D.R. Johnson.: *World Ocean Atlas 2013, Volume 4: Dissolved Inorganic Nutrients*
868 (phosphate, nitrate, silicate), S. Levitus, Ed., A. Mishonov Technical Ed.; NOAA Atlas NESDIS
869 76, 25 pp, 2014.

870 Gattuso, J. P., B. Gentili, C. M. Duarte, J. A. Kleypas, J. J. Middelburg, and D. Antoine.: Light
871 availability in the coastal ocean: Impact on the distribution of benthic photosynthetic organisms
872 and their contribution to primary production, *Biogeosciences*, 3, 489 – 513, doi:10.5194/bg-3-
873 489-2006, 2006.

874 Gent, P. R., McWilliams. J. C.: Isopycnal mixing in ocean circulation models, *J. Phys.*
875 *Oceanogr.*, 20, 150 – 155, doi: 10.1175/15200485, 1990.

876 Harwell, C., Kim, K., Burkholder, J., Colwell, R., Epstein, P. R., Grimes, D., Hofmann, E. E.,
877 Lipp, E. K., Osterhaus, A., and Overshreet, R. M.: Emerging marine diseases-climate links and
878 anthropogenic factors, *Science.*, 285(5433), 1505 – 1510, doi: 10.1126/science.285.5433.1505,
879 1999.

880 Howden, S., Murtugudde, R.: Effects of river inputs into the Bay of Bengal, *J. Geophys. Res.*,
881 106, 19,825-19,843. doi: 10.1029/2000JC000656, 2001.

882 Jerlov N. G.: *Marine optics*, Second ed., Elsevier, pp 231, 1976.

883 Jung, E., and Kirtman. B. P.: ENSO modulation of tropical Indian ocean subseasonal variability,
884 *Geophys. Res. Lett.*, 43, doi: 10.1002/2016GL071899, 2016.

885 Keeling, C. D., Whorf, T. P., Wahlen, M., and van der plicht, J.: Interannual extremes in the rate
886 of rise of atmospheric carbon dioxide since 1980, *Nature*, 375, 666 – 670, 1995.

887 Key, R. M., et al.: A global ocean carbon climatology: Results from Global Data Analysis
888 Project (GLODAP), *Global Biogeochem. Cycles*, 18, GB4031, doi:10.1029/2004GB002247,
889 2004

890 Krey, J., Bahenerd, B.: *Phytoplankton production atlas of the international Indian Ocean*
891 *expedition*, Institut fur Meereskundeander Universitat Kiel, Kiel, German, 1976.

892 Laws, E. A., P. G. Falkowski, W.O. Smith, Jr., H. Ducklow and J. J. McCarthy: Temperature
893 effects on export production in the open ocean, *Global Biogeochem. Cycles*, 14, 1231 – 1246.

894

895 Large, W. G., McWilliams, J. C., Doney, S. C.: Oceanic vertical mixing: A review and a model
896 with a nonlocal boundary layer parameterization, *Rev. Geophys.*, 32, 363 – 403, doi:
897 10.1029/94RG01872, 1994.

898 Le Quere, C., Orr, J. C., Monfray, P., Aumont, O.: Interannual variability of the oceanic sink of
899 CO₂ from 1979 through 1997, *Global Biogeochem. Cycles.*, 14, p1247 – 1265, doi:
900 10.1029/1999GB900049, 2000.

901 Lee, P. F., Chen, I. C., Tzeng, W. N.: Spatial and Temporal distributions patterns of bigeye tuna
902 (*Thunnus obesus*) in the Indian Ocean, *Zoological studies-Taipei*-, 44(2), 260, 2005.

903 Lehodey .P., Senina I., Sibert. J., Bopp. L., Calmettes B., Hampton .J., Murtugudde. R.:
904 Preliminary forecasts of Pacific bigeye tuna population trends under the A2 IPCC scenario, *Prog*
905 *in Oceanography.*, 86, 302 – 315, doi:10.1016/j.pocean.2010.04.021, 2010.

906 Liao, X., Zhan, H., Du, Y.: Potential new production in two upwelling regions of the Western
907 Arabian Sea: Estimation and comparison, *J. Geophys. Res. Oceans.*, 121,
908 doi:10.1002/2016JC011707, 2016.

909 Lopez-Urrutia, A., E. San Martin, R. P. Harris, and X. Irigoien.: Scaling the metabolic balance of
910 the oceans, *Proc. Natl. Acad. Sci. U.S.A.*, 103, 8739-8744, doi:10.1073/pnas.0601137103, 2006.

911 Louanchi. F., N. Metzl., and Alain Poisson.: Modelling the monthly sea surface f_{CO2} fields in the
912 Indian Ocean, *Marine Chemistry*, 55, 265 – 279, 1996.

913 Marra, J. F., Veronica P. Lance, Robert D. Vaillancourt, Bruce R. Hargreaves.: Resolving the
914 ocean's euphotic zone, *Deep Sea. Res. pt. I.*, 83, 45 -50, doi:10.1016/j.dsr.2013.09.005, 2014.

915 Matsumoto K., Tokos. K. S., Price., A. R., Cox. S. J.: First description of the Minnesota Earth
916 System Model for Ocean biogeochemistry (MESMO 1.0), *Geosci. Model Dev.*, 1, 1-15,
917 doi:10.5194/gmd-1-1-2008, 2008.

918 McCreary, J., Murtugude, R., Vialard, J., Vinayachandran, P., Wiggert, J. D., Hood, R. R.,
919 Shankar, D., Shetye, S.: Biophysical processes in the Indian Ocean, *Indian Ocean*
920 *Biogeochemical Processes and Ecological Variability.*, 9 – 32, doi: 10.1029/GM185, 2009.

921 Mehrbach, C., C. H. Culberson, J. E. Hawley, and R. M. Pytkowicz.: Measurement of the
922 apparent dissociation constants of carbonic acid in seawater at atmospheric pressure, *Limnol.*
923 *Oceanogr.*, 18, 897 – 907, 1973.

924 Moisan, J. R., Moisan, A. T., Abbott, M. R.: Modelling the effect of temperature on the
925 maximum growth rates of phytoplankton populations, *Eco. Modelling.*, 153, 197-215,
926 doi:10.1016/S0304-3800(02)00008, 2002.

927 Morel, A.: Optical modeling of the upper ocean in relation to its biogenous matter content (Case
928 1 Waters), *J. Geophys. Res.*, 93, 10479-10, 768, doi: 10.1029/JC093iC09p10749, 1988.

929 Murtugudde R., McCreary J. P., Busalacchi, A. J.: Oceanic processes associated with anomalous
930 events in the Indian Ocean with relevance to 1997-1998, *J. Geophys. Res.*, 105, 3295-3306, doi:
931 10.1029/1999JC900294, 2000.

932 Murtugudde, R., Busalacchi, A. J.: Interannual variability of the dynamics and thermodynamics
933 of the tropical Indian Ocean, *J. Clim.* 12, 2300-2326, doi:10.1175/1520-0442, 1999.

934 Murtugudde, R., Seager, R., Thoppil, P.: Arabian Sea response to monsoon variations,
935 *Paleoceanography.*, 22, PA4217, doi:10.1029/2007PA001467, 2007.

936 Najjar, R. G., Keeling, R. F.: Analysis of the mean annual cycle of the dissolved oxygen
937 anomaly in the world ocean, *J. Mar. Res.*, 55, 117 – 151, doi:10.1357/0022240973224481, 1997.

938 Najjar, R. G., Orr, J. C.: Design of OCMIP-2 simulations of chlorofluorocarbons, the solubility
939 pump and common biogeochemistry, <http://www.ipsl.jussieu.fr/OCMIP/>, 1998.

940 Najjar, R. G., Sarmiento, J. L., Toggweiler, J. R.: Downward transport and fate of organic matter
941 in the ocean: simulations with a general circulation model, *Global Biogeochem. Cycles.*, 6, 45-
942 76, doi/10.1029/91GB02718, 1992.

943 Naqvi, S. W. A., Moffett, J. W., Gauns, M. U., Narvekar, P. V., Pratihary, A. K., Naik, H.,
944 Shenoy, D. M., Jayakumar, D. A., Goepfert, T. J., Patra, P. K., Al-Azri, A., and Ahmed, S. I.:
945 The Arabian Sea as a high-nutrient, low-chlorophyll region during the late Southwest Monsoon,
946 *Biogeosciences.*, 7, 2091-2100, doi:10.5194/bg-7-2091-2010, 2010.

947 Naqvi, S., Naik, H., Narvekar, P.: The Arabian Sea, in *Biogeochemistry*, edited by K. Black and
948 G. Shimmield, pp. 156 – 206, Blackwell, Oxford, 2003.

949 Orr, J. C., and co-authors.: Anthropogenic ocean acidification over the twenty-first century and
950 its impact on calcifying organisms, *Nature*, 437, 681 – 686, doi:10.1038/nature04095, 2005.

951 Orr, J. C., and co-authors.: Estimates of anthropogenic carbon uptake from four three-
952 dimensional global ocean models, *Glob. Biogeochem. Cycles.*, 15, p43 – 60, doi:
953 10.1029/2000GB001273, 2001.

954 Orr, J. C., Aumont, O., Bopp, L., Calderia, K., Taylor, K., et. al.: Evaluation of seasonal air-sea
955 CO₂ fluxes in the global carbon cycle models, International open Science conference (Paris, 7-
956 10 Jan. 2003), 2003.

957 Osawa, T., Julimantoro, S.: Study of fishery ground around Indonesia archipelago using remote
958 sensing data, *International archives of the Photogrammetry, Remote sensing and spatial*
959 *information science.*, vol XXXVIII, part-8, 2010.

960 Parsons, T. R., Takahashi, M., Habgrave, B.: In *Biological Oceanographic Processes*, 3rd ed.,
961 330pp., Pergamon Press, New York, doi: 10.1002/iroh.19890740411, 1984.

962 Prasanna Kumar, .S., Muraleedharan, P. M., Prasad, T. G., Gauns, M., Ramaiah, N., de Souza, S.
963 N., Sardesai, S., Madhupratap, M.: Why is the Bay of Bengal less productive during summer
964 monsoon compared to the Arabian Sea?, *Geophys. Res. Lett.*, 29(24), 2235,
965 doi:10.1029/2002GL016013, 2002.

966 Prasanna Kumar, S., Roshin, P. R., Narvekar, J., Dinesh Kumar, P., Vivekanandan, E.: What
967 drives the increased phytoplankton biomass in the Arabian Sea?, *Current Science*, 99(I), 101 –
968 106, 2010.

969 Prassana Kumar. S, Ramaiah. N, Gauns. M., Sarma V. V. S. S., Muraleedharan. P. M.,
970 RaghuKumar. S., Dileep Kumar., Madhupratap. M.: Physical forcing of biological productivity
971 in the Northern Arabian Sea during the Northeast Monsoon, *Deep Sea Res. Pt. II.*, 48, 1115-
972 1126, doi:10.1016/S0967-0645(00)00133-8, 2001.

973 Praveen, V., Ajayamohan, R. S., Valsala, V., Sandeep, S.: Intensification of upwelling along
974 Oman coast in a warming scenario, *Geophys. Res. Lett.*, 43, doi:10.1002/2016GL069638, 2016.

975 Qasim, S. Z.: Biological productivity of the Indian Ocean, *J. Mar. Sci.*, 6, 122 – 137, 1977.

976 Qasim, S. Z.: Oceanography of Northern Arabian Sea, *Deep Sea Res.*, 29(9A), 1041 – 1068,
977 doi:10.1016/0198-0149(82)90027-9, 1982.

978 Redi, M.: Oceanic isopycnal mixing by coordinate rotation, *J. Phys. Oceanogr.*, 12, 1154 – 1158,
979 doi: 10.1175/1520-0485, 1982.

980 Regaudie-de-Gioux, A., and C. M. Duarte.: Compensation irradiance for planktonic community
981 metabolism in the ocean, *Global Biogeochem. Cycles*, 24, GB4013,
982 doi:10.1029/2009GB003639, 2010.

983 Roxy, M. K., Modi, A., Murtugudde, R., Valsala, V., Panickal, S., Prasanna Kumar, S.,
984 Ravichandran, M., Vichi, M., Levy, M.: A reduction in marine primary productivity driven by
985 rapid warming over the tropical Indian Ocean, 43, 826 – 833, *J. Geophys. Res. Letters.*,
986 doi:10.1002/2015GL066979, 2015.

987 Ryther, J., Menzel, D.: On the production, composition, and distribution of organic matter in the
988 Western Arabian Sea, *Deep Sea Research and Oceanographic Abstracts.*, 12(2), 199 -209.
989 doi:10.1016/0011-7471(65)90025-2, 1965.

990 Ryther, J.: Photosynthesis in the ocean as function of light Intensity, *Limnol. Oceanogr.*, vol 1,
991 issue 1, doi: 10.4319/lo.1956.1.1.0061, 1956.

992 Sarma V. V. S. S.: Net plankton community production in the Arabian Sea based on O₂ mass
993 balance model, *Glob. Biogeochem. Cycles.*, 18, GB4001, doi:10.1029/2003GB002198, 2004.

994 Sarma, V. V. S. S.: An evaluation of physical and biogeochemical processes regulating the
995 perennial suboxic conditions in the water column of the Arabian Sea, *Global Biogeochem.*
996 *Cycles.*, 16, doi:10.1029/2001GB001461, 2002.

997 Sarmiento, J. L., and Gruber, N.: *Ocean Biogeochemical Dynamics*, Princeton University Press,
998 New Jersey, 2006.

999 Sarmiento, J. L., Monfray. P., Maier-Reimer., Aumont, O., Murnane, R. J., Orr, J. C.: Sea-air
1000 CO₂ fluxes and carbon transport: A comparison of three ocean general circulation models,
1001 *Global Biogeochem. Cycles.*, 14, p1267 – 1281. doi: 10.1029/1999GB900062, 2000.

1002 Schott, F.: Monsoon response of the Somali current and associated upwelling, *Prog.Oceanogr.*,
1003 12, 357 – 381, doi:10.1016/0079-6611(83)90014-9, 1983.

1004 Smetacek, V., and Passow, U.: Spring bloom initiation and Sverdrup's critical depth model,
1005 *Limnol. Oceanogr.*, 35, 228 – 234, doi: 10.4319/lo.1990.35.1.0228, 1990.

1006 Smith, L. S.: Understanding the Arabian Sea: Reflections on the 1994-1996 Arabian Sea
1007 Expedition, *Deep Sea Res. Pt. II.*, 48, 1385-1402, doi:10.1016/S0967-0645(00)00144-2, 2001.

1008 Smith, R. L., Bottero, L. S.: On upwelling in the Arabian Sea. In Angel, M (ed) *A voyage of*
1009 *Discovery*. Pergamon Press, New York, p. 291 – 304, 1977.

1010 Smith, S. L., Codispoti, L. A.: Southwest monsoon of 1979: chemical and biological response of
1011 Somali coastal waters. *Science*, 209, 597 – 600. doi:10.1126/science.209.4456.597, 1980.

1012 Smith, S. L.: Biological indications of active upwelling in the northwestern Indian Ocean in 1964
1013 and 1979, a comparison with Peru and northwest Africa, *Deep Sea Res.*, 31, 951 – 967,
1014 doi:10.1016/0198-0149(84)90050-5, 1984.

1015 Susanto. R., Gordon, A. L., Zheng. Q.: Upwelling along the coasts of Java and Sumatra and its
1016 relation to ENSO, *J. Geophys. Res. Lett.*, 28, 1599-1602, doi: 10.1029/2000GL011844, 2001.

1017 Swallow, J. C.: Some aspects of the physical oceanography of the Indian Ocean, *Deep Sea Res.*,
1018 31, 639 – 650, doi:10.1016/0198-0149(84)90032-3, 1984.

1019 Takahashi, T., Sutherland, S. C., Wanninkhof, R., Sweeney, C., Feely, R. A., Chipman, D. W.,
1020 Hales, B., Friederich, G., Chavez, F., Sabine, C., et al.: Climatological mean and decadal
1021 changes in surface ocean pCO₂ and net sea-air CO₂ flux over the global oceans. *Deep Sea Res.*,
1022 Pt. II., 56, 554 – 557, doi:10.1016/j.dsr2.2008.12.009, 2009.

1023 Valsala V., R. R. Rao.: Coastal Kelvin waves and dynamics of gulf of Aden eddies, *Deep Sea*
1024 *Res.*, Pt. I., 116, 174 – 186, <https://doi.org/10.1016/j.dsr.2016.08.003>, 2016.

1025 Valsala V., Maksyutov, S.: A short surface pathway of the subsurface Indonesian Throughflow
1026 water from the Java Coast associated with upwelling, Ekman Transport, and Subduction. *Int. J.*
1027 *Oceanogr.*, 15, doi: 10.1155/2010/540743, 2010.

1028 Valsala V., Maksyutov, S.: Interannual variability of air-sea CO₂ flux in the north Indian Ocean,
1029 *Ocean Dynamics.*, 1 – 14, doi 10.1007/s10236-012-0588-7, 2013.

1030 Valsala, K. V., Maksyutov, S., Ikeda, M.: Design and Validation of an offline oceanic tracer
1031 transport model for a carbon cycle study, *J. clim.*, 21, doi: 10.1175/2007JCLI2018.1, 2008.

1032 Valsala, V., Maksyutov, S., Murtugudde, R.: Interannual to Interdecadal Variabilities of the
1033 Indonesian Throughflow Source Water Pathways in the Pacific Ocean, *J. Phys. Oceanogr.*, 41,
1034 1921–1940, doi: 10.1175/2011JPO4561.1, 2011.

1035 Valsala, V., Maksyutov, S.: Simulation and assimilation of global ocean pCO₂ and air-sea CO₂
1036 fluxes using ship observations of surface ocean pCO₂ in a simplified biogeochemical model,
1037 *Tellus.*, 62B, doi: 10.1111/j.1600-0889.2010.00495, 2010.

1038 Valsala, V., Murtugudde, R.: Mesoscale and Intraseasonal Air-Sea CO₂ Exchanges in the
1039 Western Arabian Sea during Boreal Summer, *Deep Sea Res. Pt. I*, 103, 103-113,
1040 doi:10.1016/j.dsr.2015.06.001, 2015.

1041 Valsala, V., Roxy, M., Ashok, K., Murtugudde, R.: Spatio-temporal characteristics of seasonal to
1042 multidecadal variability of pCO₂ and air-sea CO₂ fluxes in the equatorial Pacific Ocean, *J.*
1043 *Geophys. Res.*, 119, 8987 – 9012, doi:10.1002/2014JC010212, 2014.

1044 Valsala, V.: Different spreading of Somali and Arabian coastal upwelled waters in the northern
1045 Indian Ocean: A case study. *J. Phy. Oceanogr.*, 803 – 816, doi: [https://doi.org/10.1007/s10872-](https://doi.org/10.1007/s10872-009-0067-z)
1046 [009-0067-z](https://doi.org/10.1007/s10872-009-0067-z), 2009.

1047 Vialard, J. and co-authors.: Air-Sea Interactions in the Seychelles-Chagos Thermocline Ridge
1048 Region, *BAMS*, doi:10.1175/2008BAMS2499.1, 2009.

1049 Vinayachandran P. N., Shankar D., S. Vernekar, K. K. Sandeep, P. Amol, C. P. Neema and A.
1050 Chatterjee.: A summer monsoon pump to keep the bay of Bengal salty, *Geophys. Res. Lett.*, 40,
1051 1777 – 1782, doi:10.1002/grl.50274, 2013.

1052 Vinayachandran P. N., Yamagata, T.: Monsoon Response of the Sea around Sri Lanka:
1053 Generation of Thermal Domes and Anticyclonic Vortices, *J. Phy. Oceano.*, 28, 1946 – 1960, doi:
1054 10.1175/1520-0485, 1998.

1055 Vinayachandran, P. N., Chauhan, P., Mohan, M., Nayak, S.: Biological response of the sea
1056 around Sri Lanka to summer monsoon, *Geophys. Res. Lett.*, 31, L01302,
1057 doi:10.1029/2003GL018533, 2004.

1058 Wang .X. J., Behrenfeld. M., Le Borgne .R., Murtugudde .R., and Boss. E.: Regulation of
1059 phytoplankton carbon to chlorophyll ratio by light, nutrients and temperature in the equatorial
1060 Pacific Ocean: a basin-scale model. *Biogeosciences.*, 6, 391 – 404, doi:10.5194/bg-6-391-2009,
1061 2009.

1062 Weiss, R. F.: Carbon dioxide in water and seawater: The solubility of a non-ideal gas, *Mar.*
1063 *Chem.*, 2, 203-215, 1974.

1064 Wiggert J. D., Jones. B. H., Dickey .T D., Brink .K. H., Weller .R .A., Marra. J., Codispoti. L.
1065 A.: The Northeast Monsoon's impact on mixing, phytoplankton biomass and nutrient cycling in
1066 the Arabian Sea, *Deep Sea Res. Pt. II*, 47, 1353-1385, doi:10.1016/S0967-0645(99)00147-2,
1067 2000.

1068 Wiggert, J. D., Hood, R. R., Banse, K., Kindle, J. C.: Monsoon-driven biogeochemical processes
1069 in the Arabian Sea, *Progr. Oceanogr.*, 65, 176-213, doi:10.1016/j.pocean.2005.03.008, 2005.

1070 Wiggert. J. D., Murtugudde, R. G., Christian J. R.: Annual ecosystem variability in the tropical
1071 Indian Ocean: results of a coupled bio-physical ocean general circulation model, *Deep Sea Res.*
1072 *Pt. II.*, 53, 644-676, doi:10.1016/j.dsr2.2006.01.027, 2006.

1073 Xie, S. P., Annamalai, H., Schott, F. A., McCreary Jr. J. P.: Structure and mechanism of south
1074 Indian ocean climate variability, *J. clim.*, 15, 864 – 878, doi: 10.1175/1520-0442, 2002.

1075 Xing W., Xiaomei. L., Haigang Z., Hailong. L.: Estimates of potential new production in the
1076 Java-Sumatra upwelling system, *Chinese Journal of Oceanology and Limnology.*, 30, 1063-
1077 1067, doi:10.1007/s00343-012-1281, 2012.

1078 Yamanaka, Y., Yoshie, N, Masahiko Fujii, Maka .N. Aita and Kishi. M. J.: An Ecosystem
1079 coupled with Nitrogen-Silicon-Carbon cycles applied to station A7 in the Northwestern Pacific,
1080 J. of Oceanogr., 60, p227-241, doi: 10.1023/B:JOCE.0000038329.91976.7d, 2004.

1081 Zhou X., Weng. E., Luo., Y.: Modelling patterns of nonlinearity in the ecosystem responses to
1082 temperature, CO₂ and precipitation changes, Eco. Appli., 18, 453 – 466, doi: 10.1890/07-0626.1,
1083 2008.

1084

1085

Table: 1 WAS = Western Arabian Sea, SLD = Sri Lanka Dome, SC = Sumatra Coast, SCTR = Seychelles-Chagos Thermocline Ridge. JJAS mean and the climatological annual mean of CO₂ flux from Takahashi observations, constZc, and varZc simulations. Units are mol m⁻² yr⁻¹.

Regions	CO ₂ flux (mol m ⁻² yr ⁻¹)					
	JJAS Mean			Annual Mean		
	OBS	constZc	varZc	OBS	constZc	varZc
WAS	1.99	1.44 ± 0.2	2.31 ± 0.4	0.94	0.80 ± 0.1	1.07 ± 0.2
SLD	1.79	-0.008 ± 0.2	0.24 ± 0.09	0.8	-0.02 ± 0.1	0.10 ± 0.2
SC	0.31	0.60 ± 0.5	1.51 ± 1.01	0.21	0.21 ± 0.3	0.53 ± 0.5
SCTR	0.82	-0.32 ± 0.3	-0.05 ± 0.4	0.55	-0.02 ± 0.1	-0.07 ± 0.2

Table: 2 Same as Table 1, but for pCO₂. Units are µatm.

Regions	pCO ₂ (µatm)					
	JJAS Mean			Annual Mean		
	OBS	constZc	varZc	OBS	constZc	varZc
WAS	397.58	389.18 ± 3.7	399.95 ± 5.01	394.69	389.62 ± 3.9	391.19 ± 4.7
SLD	382.44	371.67 ± 6.04	379.24 ± 8.9	380.21	370.76 ± 6.1	374.94 ± 9.6
SC	372.52	382.36 ± 12.7	402.14 ± 21.8	372.69	374.65 ± 9.3	381.76 ± 13.6
SCTR	377.18	365.71 ± 5.08	370.72 ± 7.4	379.89	372.69 ± 4.7	369.00 ± 5.4

Table: 3 JJAS mean and the climatological annual mean of export production from satellite-derived Net Primary Production data, constZc, and varZc simulations. Units are $\text{g C m}^{-2} \text{yr}^{-1}$.

Regions	Export Production ($\text{g C m}^{-2} \text{yr}^{-1}$)					
	JJAS Mean			Annual Mean		
	OBS	constZc	varZc	OBS	constZc	varZc
WAS	123.57	84.81 ± 16.04	147.19 ± 23.8	94.31	77.41 ± 15.1	122.54 ± 25.2
SLD	51.54	167.71 ± 59.04	151.51 ± 46.4	43.25	144.43 ± 49.8	156.08 ± 43.8
SC	58.87	260.11 ± 104.7	310.03 ± 99.5	54.53	172.52 ± 72.4	215.52 ± 70.8
SCTR	51.08	57.39 ± 14.2	99.23 ± 21.8	40.45	55.15 ± 17.9	80.35 ± 26.04

Table: 4 Model derived values for New production. Units are $\text{g C m}^{-2} \text{yr}^{-1}$.

Regions	New Production ($\text{g C m}^{-2} \text{yr}^{-1}$)					
	JJAS Mean			Annual Mean		
	OBS	constZc	varZc	OBS	constZc	varZc
WAS	--	150.84 ± 27.9	133.03 ± 19.5	--	108.43 ± 23.4	81.47 ± 15.7
SLD	--	141.93 ± 64.1	77.78 ± 27.6	--	111.05 ± 71.1	50.37 ± 26.3
SC	--	63.64 ± 30.9	78.11 ± 29.1	--	56.69 ± 43.3	54.58 ± 23.3
SCTR	--	12.17 ± 16.3	13.32 ± 18.6	--	13.74 ± 15.5	12.94 ± 13

Table 5: Biological pump impact over DIC in the model due to constZc and varZc simulations for JJAS and annual mean.

Regions	Biological Pump (g C m ⁻² yr ⁻¹)			
	constZc		varZc	
	JJAS Mean	Annual Mean	JJAS Mean	Annual Mean
WAS	45.18 ± 14.8	45.49 ± 14.38	151.7 ± 23.8	126.67 ± 24.3
SLD	89.39 ± 58.1	108.65 ± 48.6	156.07 ± 48.4	161.15 ± 43.5
SC	235.54 ± 95.4	155.21 ± 67.4	319.16 ± 94.9	222.92 ± 68.7
SCTR	30.49 ± 13.4	26.81 ± 16.8	103.13 ± 19.6	83.98 ± 23.6

Table 6: Same as Table 5, But for Solubility pump.

Regions	Solubility Pump (g C m ⁻² yr ⁻¹)			
	constZc		varZc	
	JJAS Mean	Annual Mean	JJAS Mean	Annual Mean
WAS	17.29 ± 3.5	9.63 ± 2.1	27.72 ± 4.8	12.92 ± 2.7
SLD	-0.09 ± 2.4	-0.32 ± 2.3	2.9 ± 3.5	1.31 ± 3.5
SC	7.22 ± 6.9	2.56 ± 3.8	18.17 ± 12.1	6.43 ± 6.0
SCTR	-3.95 ± 3.7	-0.35 ± 2.3	-0.61 ± 5.3	-0.86 ± 2.8

Table 7: JJAS mean and climatological annual mean response from the model forced with annual mean currents.

	WAS region forced with Annual Mean Currents					
	JJAS mean			Climatological annual mean		
	constZc	varZc	Improvement	constZc	varZc	Improvement
CO ₂ flux (mol m ⁻² yr ⁻¹)	0.80 ± 0.2	1.29 ± 0.2	0.48 ± 0.04	0.65 ± 0.1	0.79 ± 0.1	0.13 ± 0.02
pCO ₂ (µatm)	381.81 ± 3.4	387.24 ± 3.9	5.43 ± 0.5	388.68 ± 3.4	388.40 ± 3.6	-0.28 ± 0.1
Export production (g C m ⁻² yr ⁻¹)	60.71 ± 4.7	104.22 ± 13.4	43.51 ± 8.6	74.30 ± 4.5	104.58 ± 18.3	30.28 ± 13.7
New Production (g C m ⁻² yr ⁻¹)	34.76 ± 2.3	52.16 ± 1.51	17.39 ± 0.8	29.91 ± 1.7	44.72 ± 1.6	14.81 ± 0.1

Table 8 Same as Table 7 but from annual mean temperature simulation.

	WAS region forced with Annual mean temperature					
	JJAS mean			Climatological annual mean		
	constZc	varZc	Improvement	constZc	varZc	Improvement
CO ₂ flux (mol m ⁻² yr ⁻¹)	1.85 ± 0.2	2.74 ± 0.4	0.88 ± 0.1	0.81 ± 0.1	1.10 ± 0.2	0.28 ± 0.07
pCO ₂ (µatm)	393.20 ± 3.01	404.26 ± 4.9	11.05 ± 1.9	384.61 ± 3.3	386.52 ± 4.8	1.91 ± 1.4

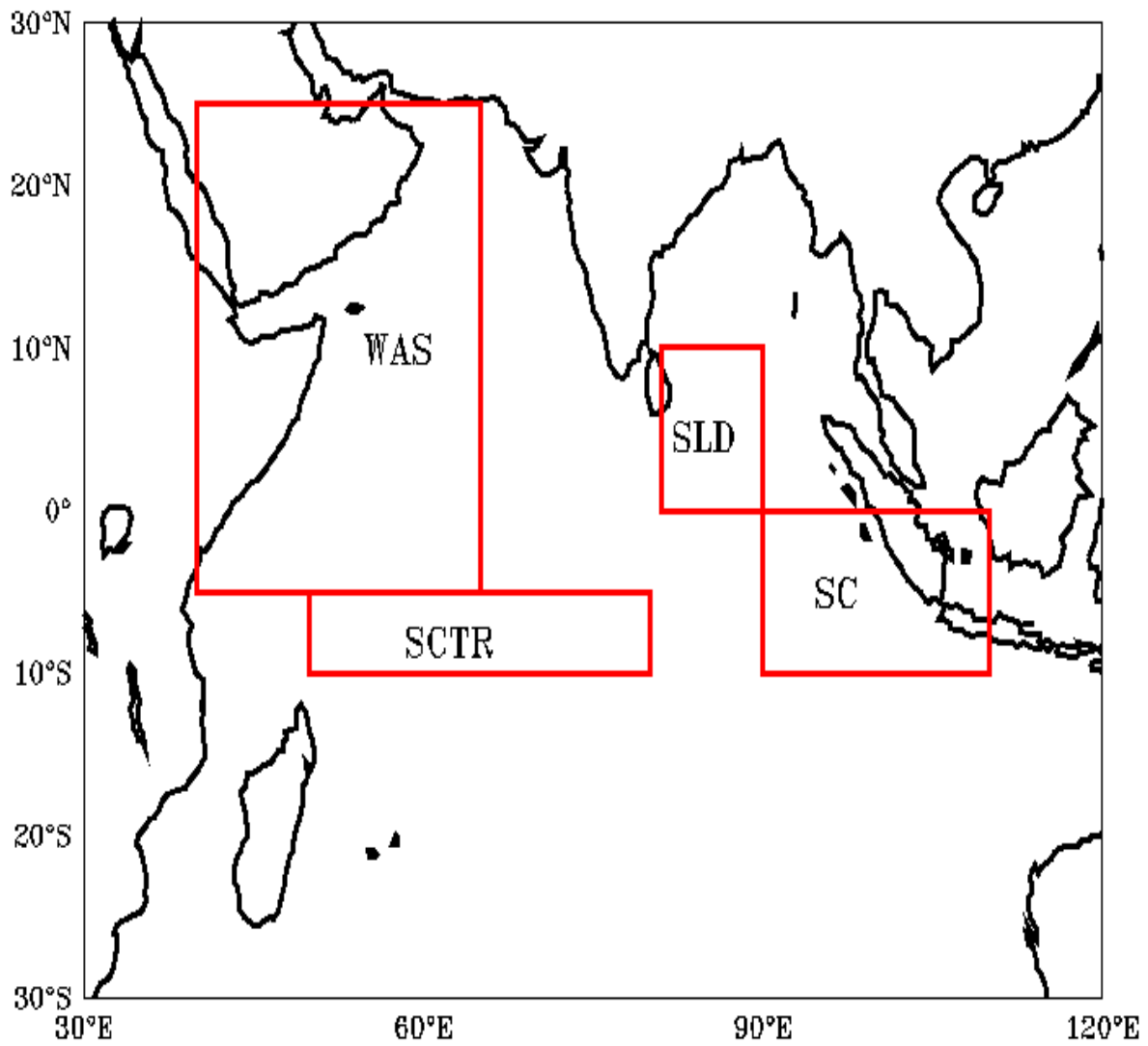


Figure 1: Red boxes shows the study regions (1) WAS (Western Arabian Sea, 40°E:65°E, 5°S:25°N) (2) SLD (Sri Lanka Dome, 81°E:90°E, 0°:10°N) (3) SCTR (Seychelles-Chagos Thermocline Ridge, 50°E:80°E, 5°S:10°S) and (4) SC (Sumatra Coast, 90°E:110°E, 0°:10°S).

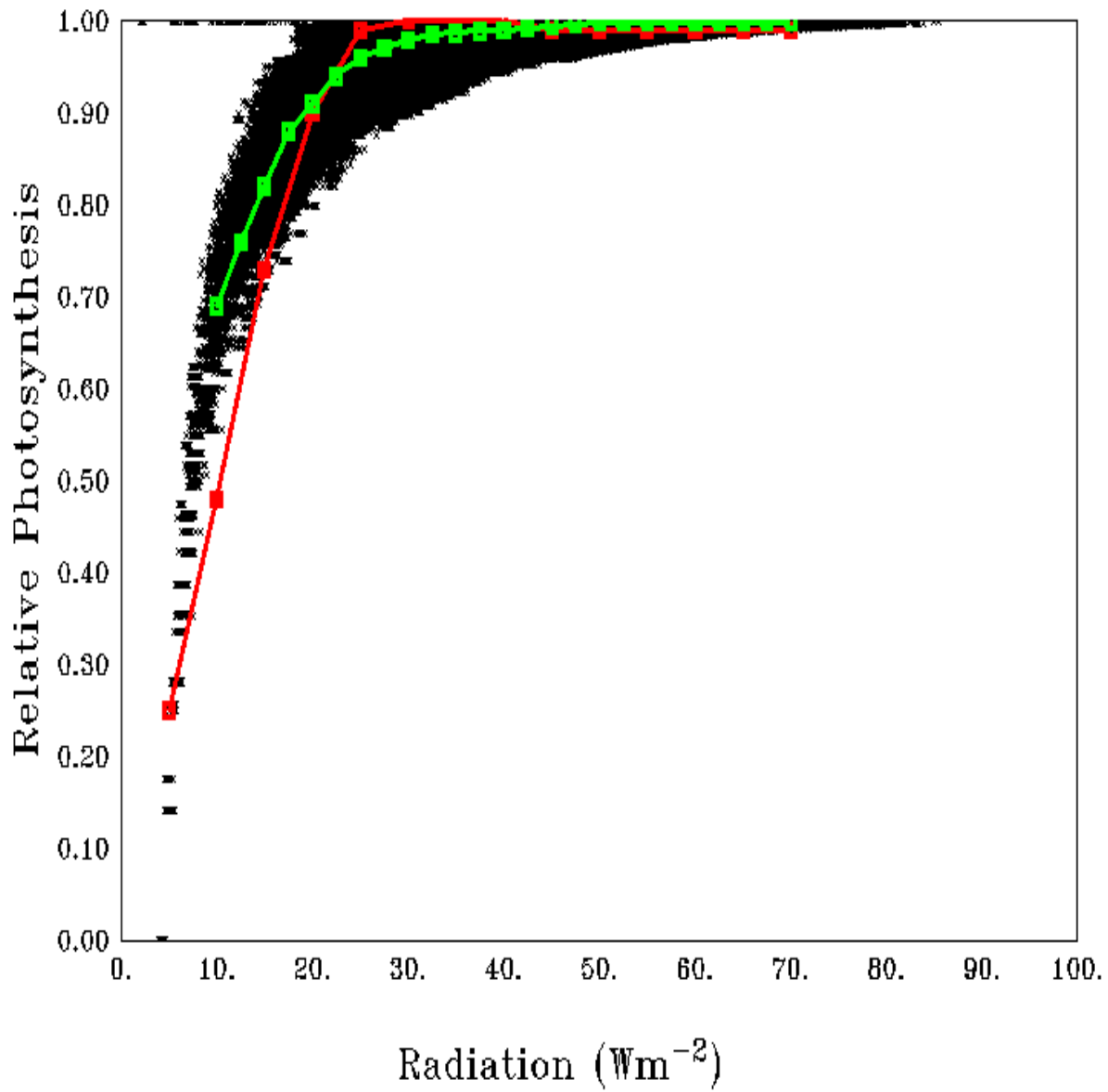


Figure 2: Scatter of average relative photosynthesis versus different light intensities in the model (black dots) and its mean (green curve). The red curve shows the theoretical P – I curve from Parsons et al., (1984).

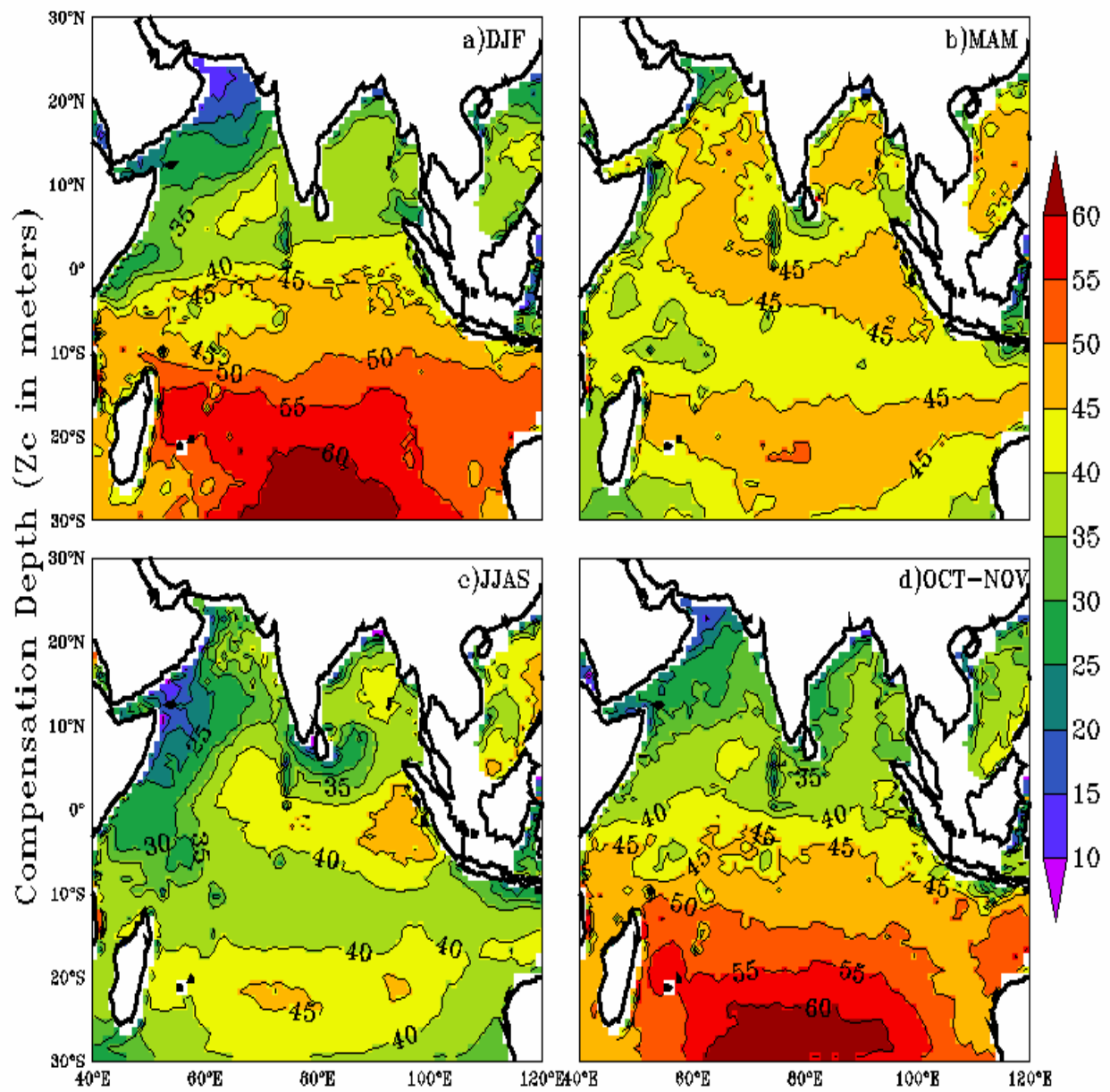


Figure 3: Seasonal-mean maps of varying compensation depth ($\text{var}Z_c$), (a) December to February (DJF), (b) March to May (MAM), (c) June to September (JJAS), (d) October to November (OCT-NOV). Units are meters.

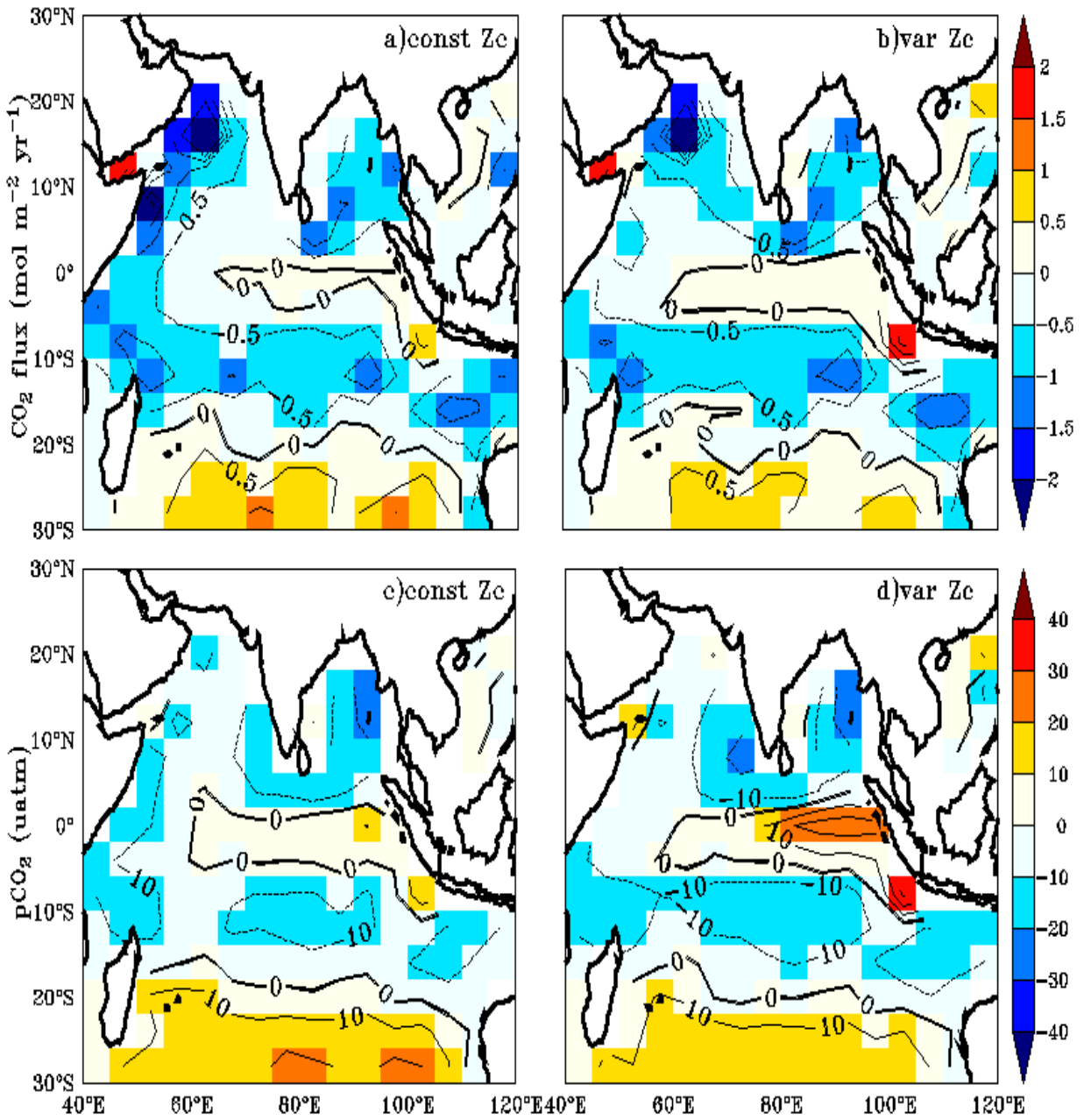


Figure 4: Annual mean biases in the model evaluated against Takahashi et al. (2009) observations for CO₂ flux (a, b) and pCO₂ (c, d) with constant Z_c (constZc) and varying Z_c (varZc). Units of CO₂ flux and pCO₂ are mol m⁻² yr⁻¹ and µatm, respectively.

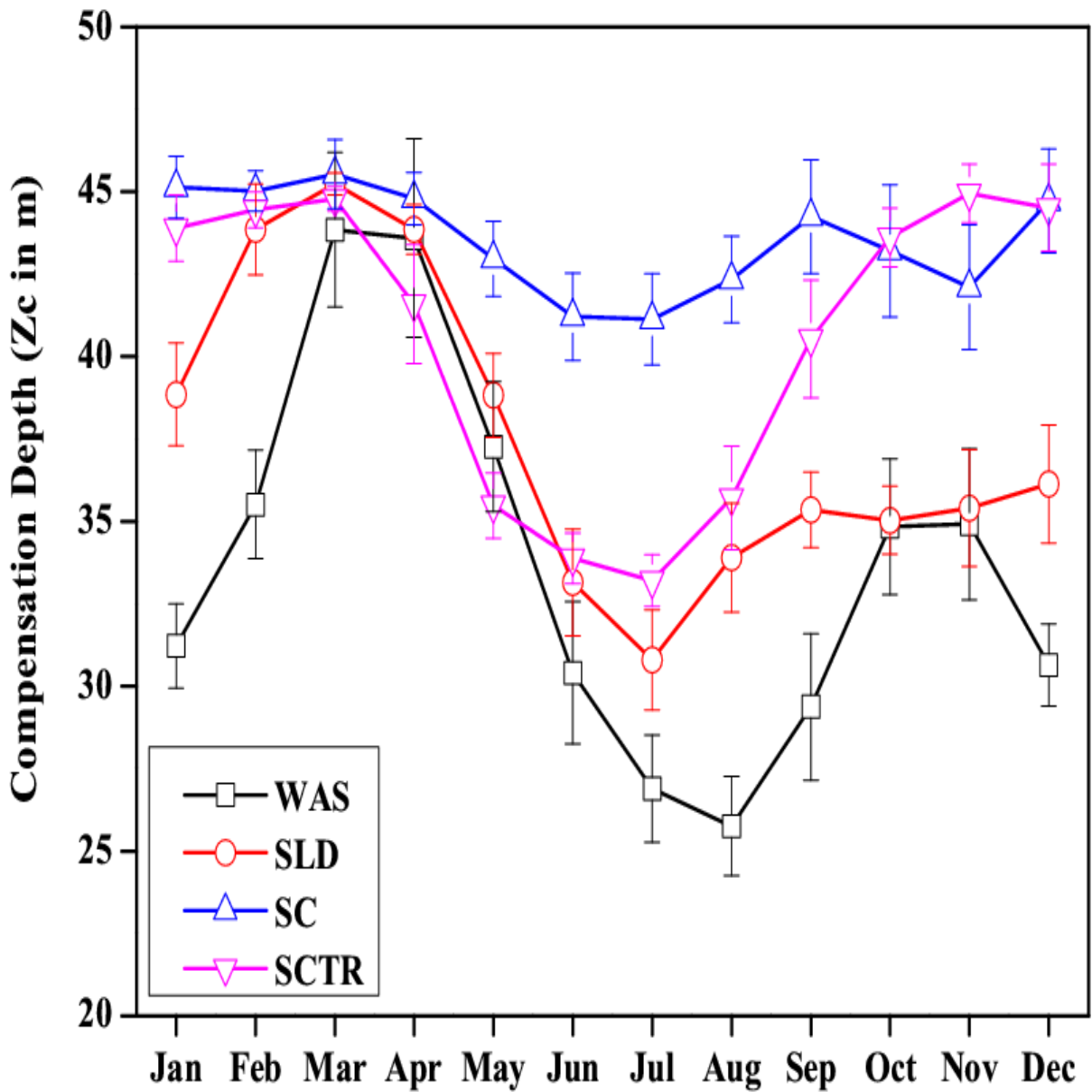


Figure 5: Seasonal variations in varZc over the study regions shown as climatology computed over 1990-2010. Error bar shows standard deviations of individual months over these years. Units are meters.

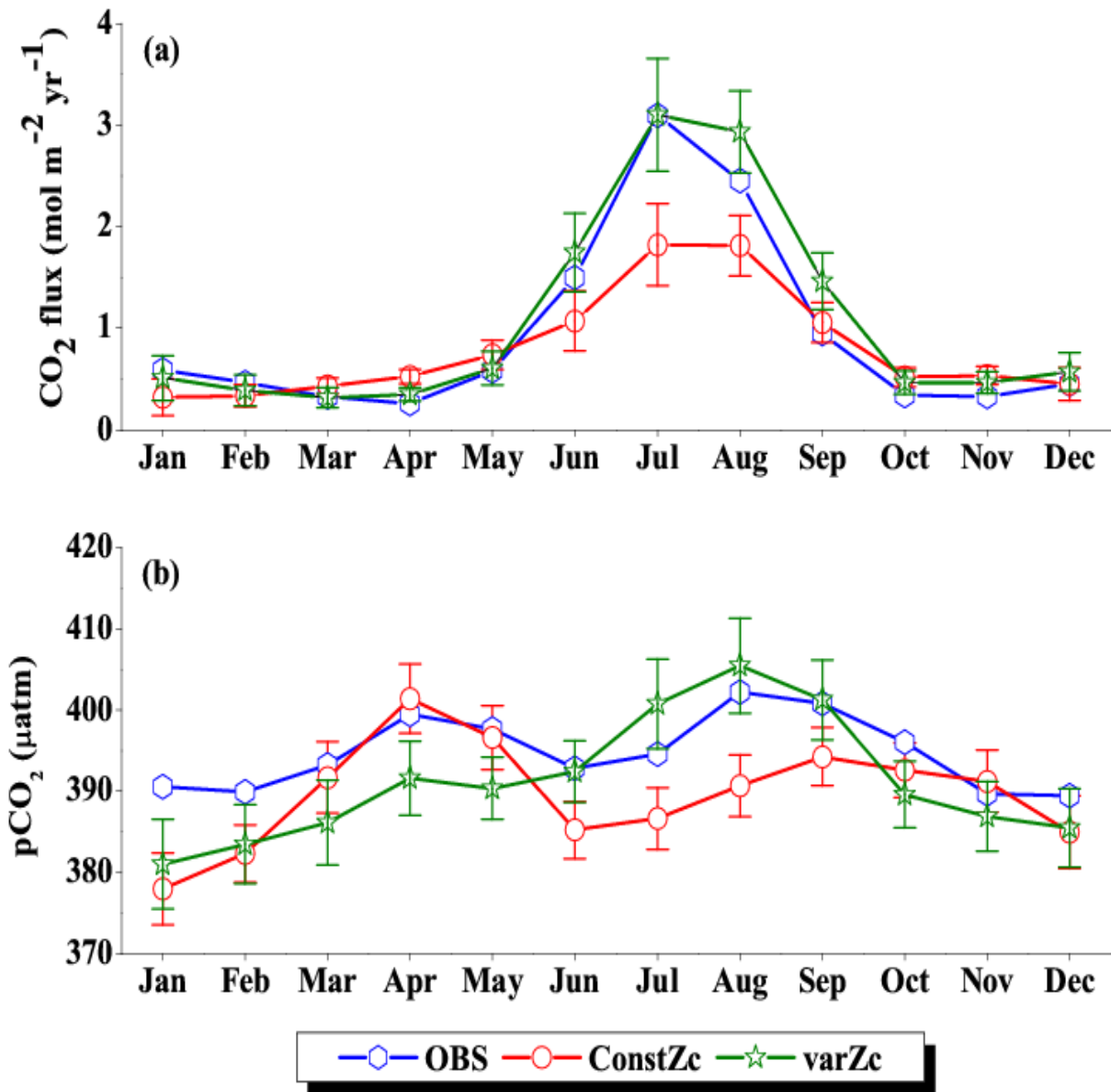


Figure 6: Comparison of model (a) CO₂ flux and (b) pCO₂ simulated with constZc and varZc with that of Takahashi et al. (2009) observations (OBS) over WAS as climatology computed over 1990-2010. Error bar shows standard deviations of individual months over these years. Units of CO₂ flux and pCO₂ are mol m⁻² yr⁻¹ and µatm, respectively. Legend is common for both graphs.

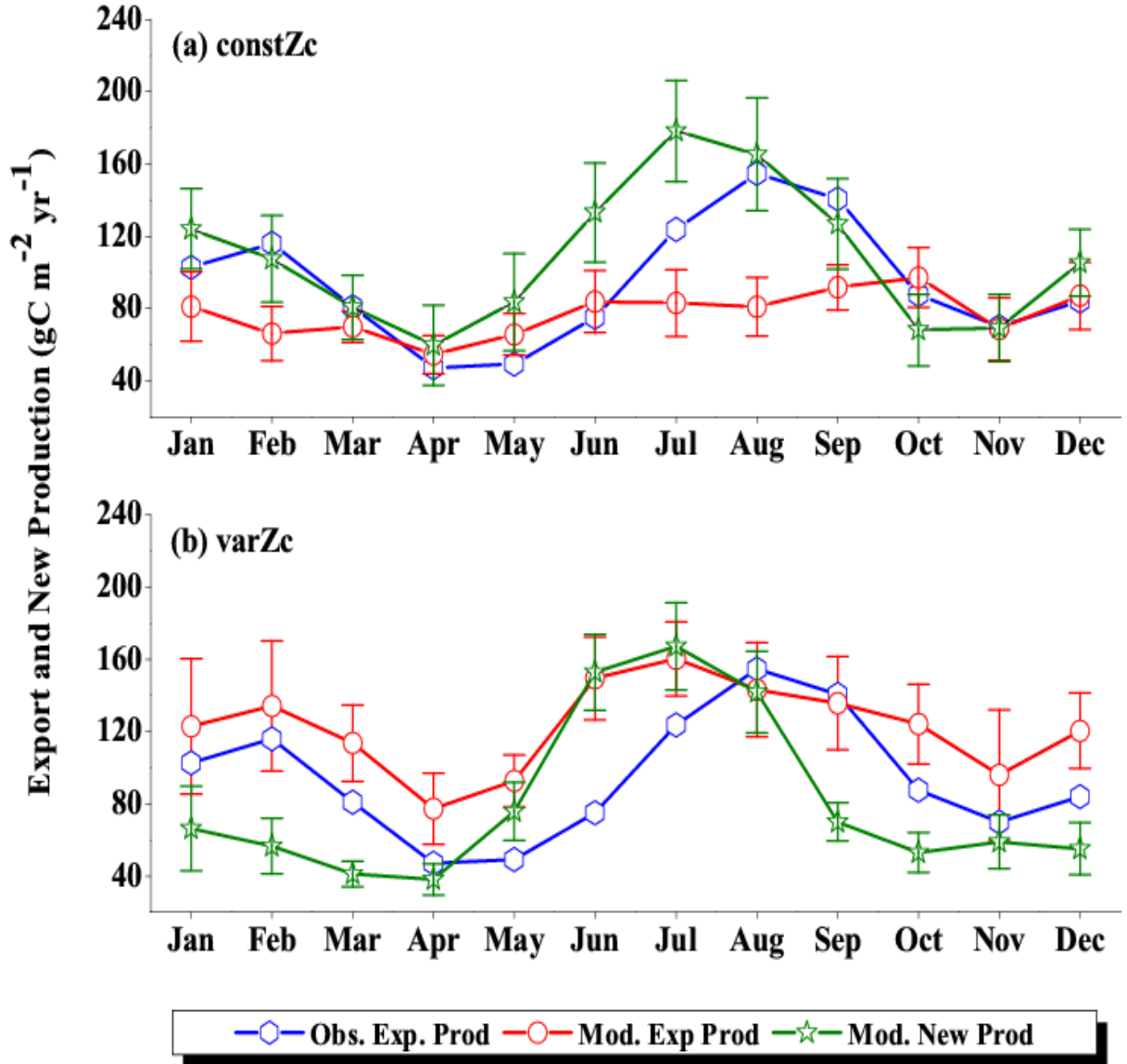


Figure 7: Comparison of model export production (Mod. Exp. Prod) and new production (Mod. New Prod) with satellite-derived export production (Obs. Exp. Prod) for (a) ConstZc and (b) varZc simulations for WAS. Units are $\text{g C m}^{-2} \text{ yr}^{-1}$. Legends are common for both graphs.

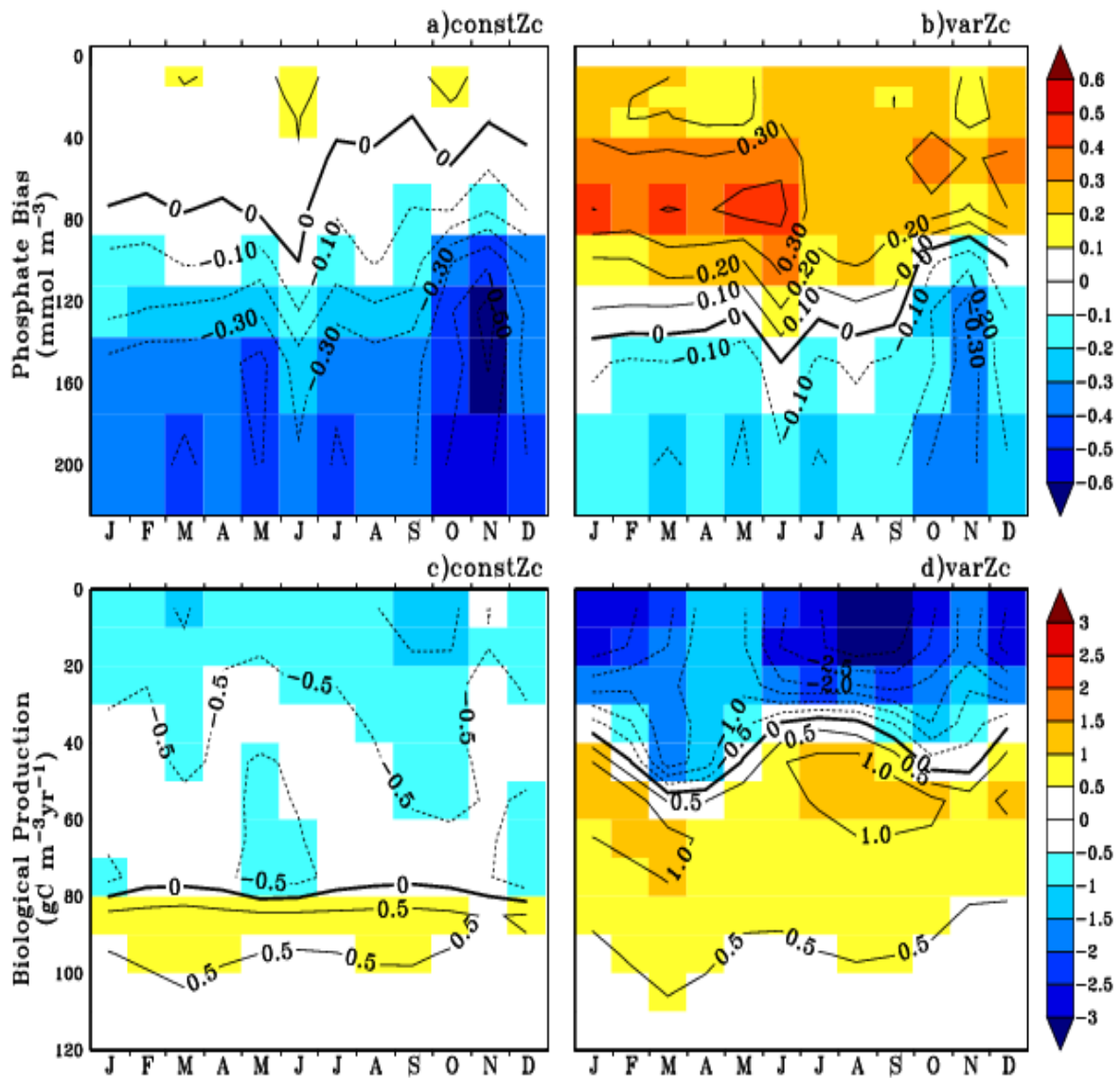


Figure 8: Annual mean bias of model phosphate when compared with climatological observational data (a) for constZc and (b) for varZc simulations. Corresponding annual mean biological source/sink profiles (c, d) in the model for WAS. Unit of phosphate is mmol m^{-3} and biological source/sink is $\text{g C m}^{-3}\text{yr}^{-1}$.

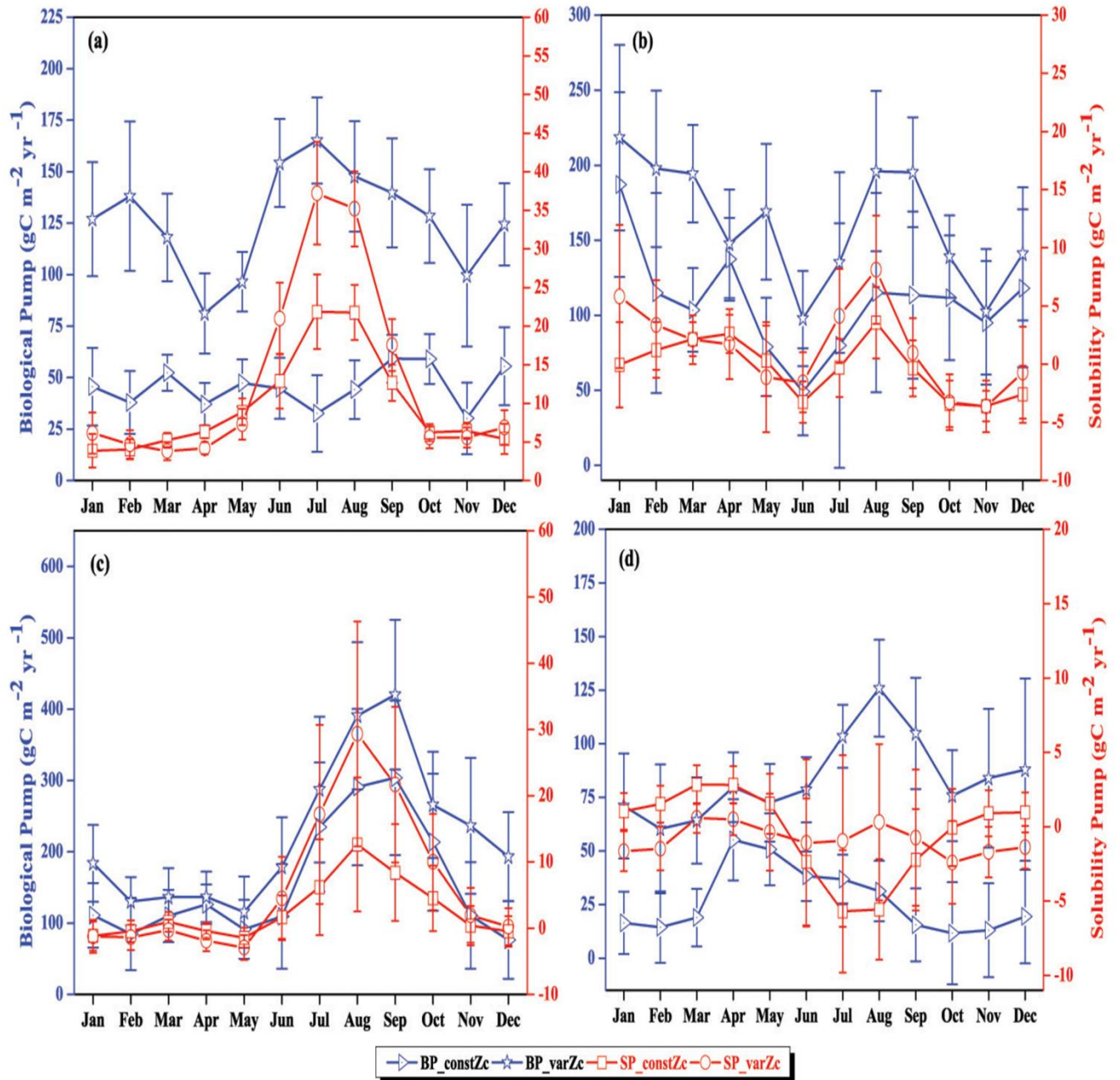


Figure 9: The strength of the biological pump (BP, black lines) and solubility pump (SP, red lines) from constZc and varZc simulations for (a) WAS (b) SLD (c) SC and (d) SCTR. The left axis shows the biological pump and the right axis shows the solubility pump. Error bar shows standard deviations of individual months over the years 1990 - 2010. Units are g C m⁻² yr⁻¹.

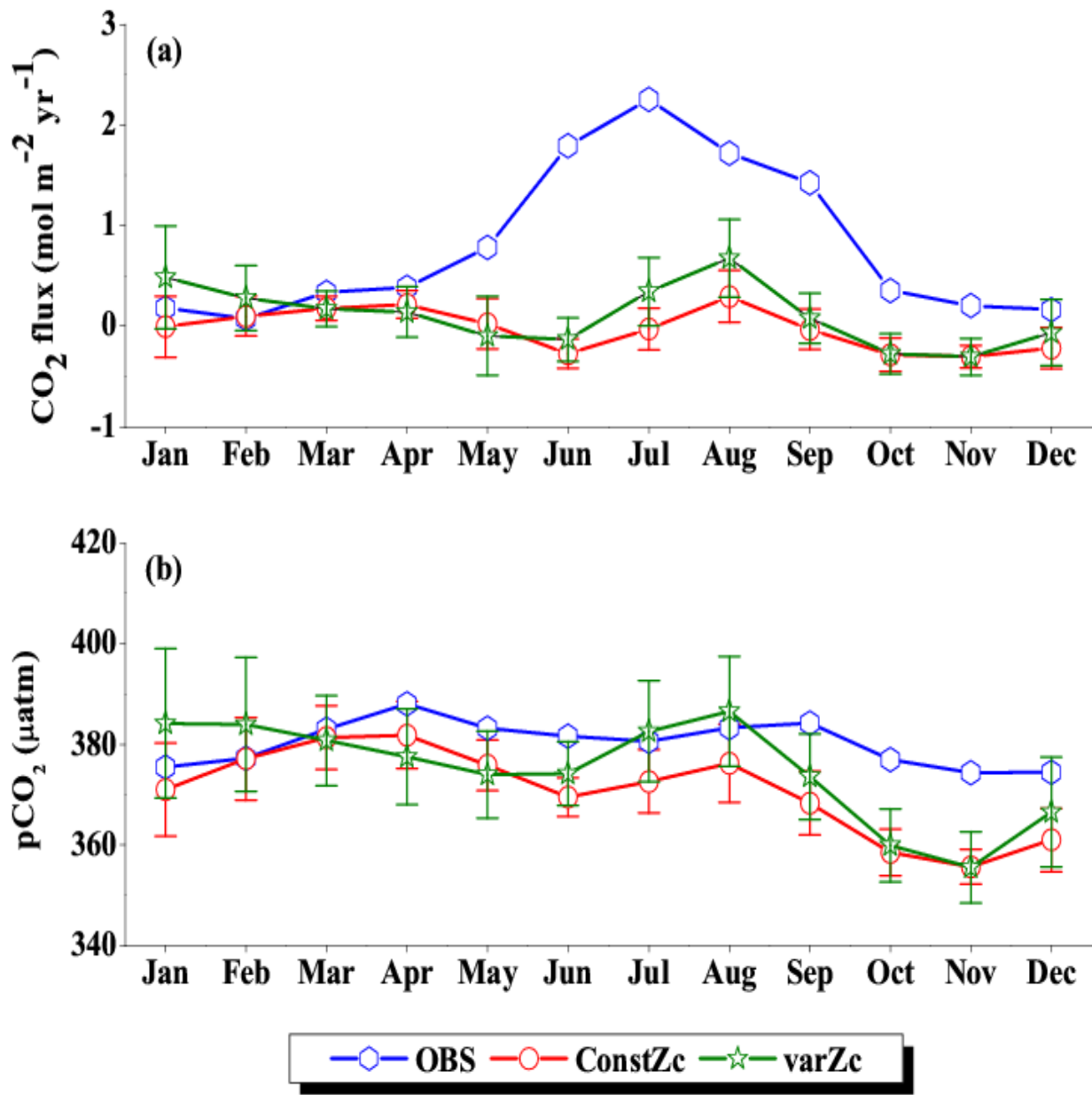


Figure 10: Same as Figure (6), but for SLD.

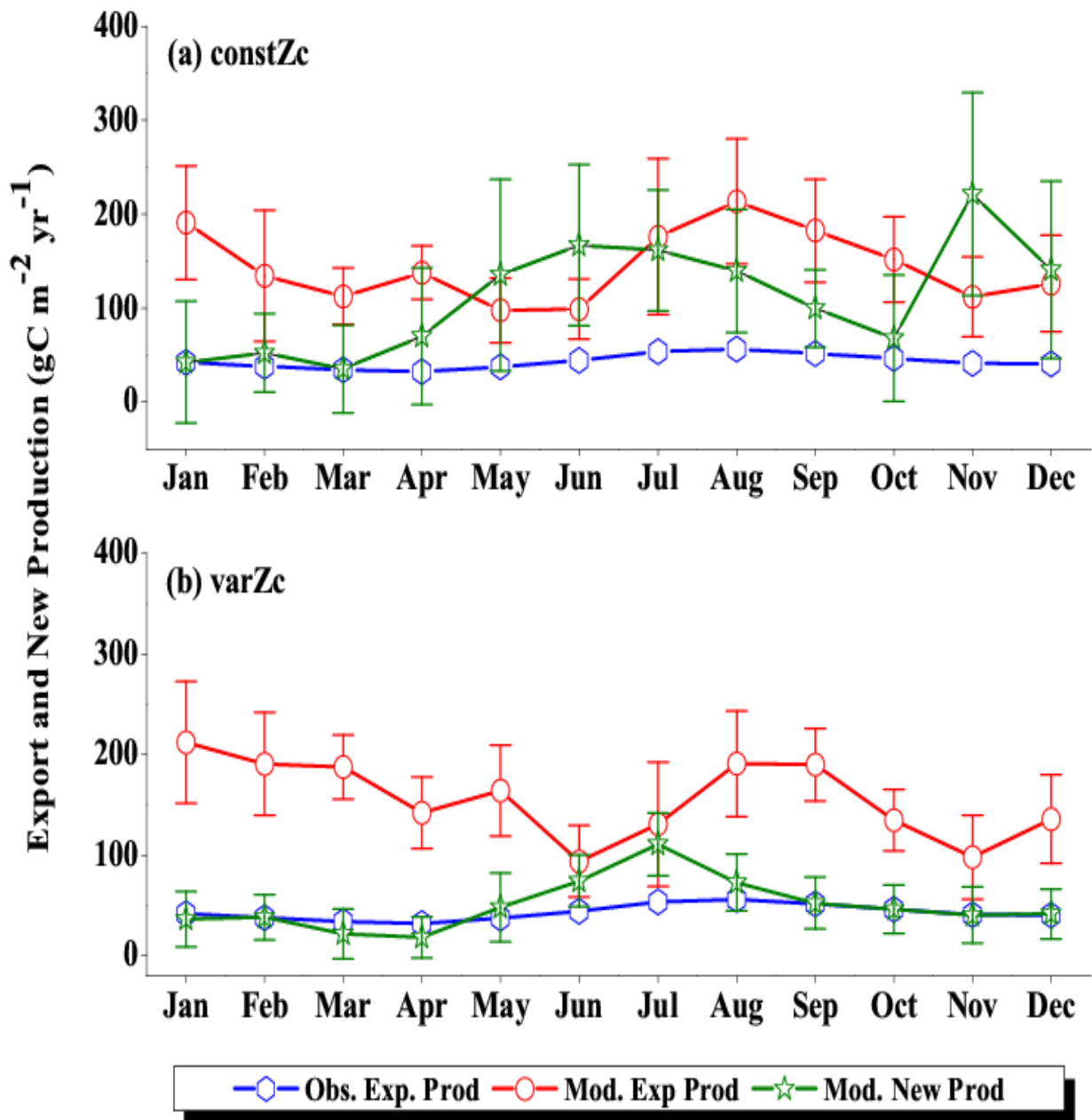


Figure 11: Same as Figure (7), but for SLD.

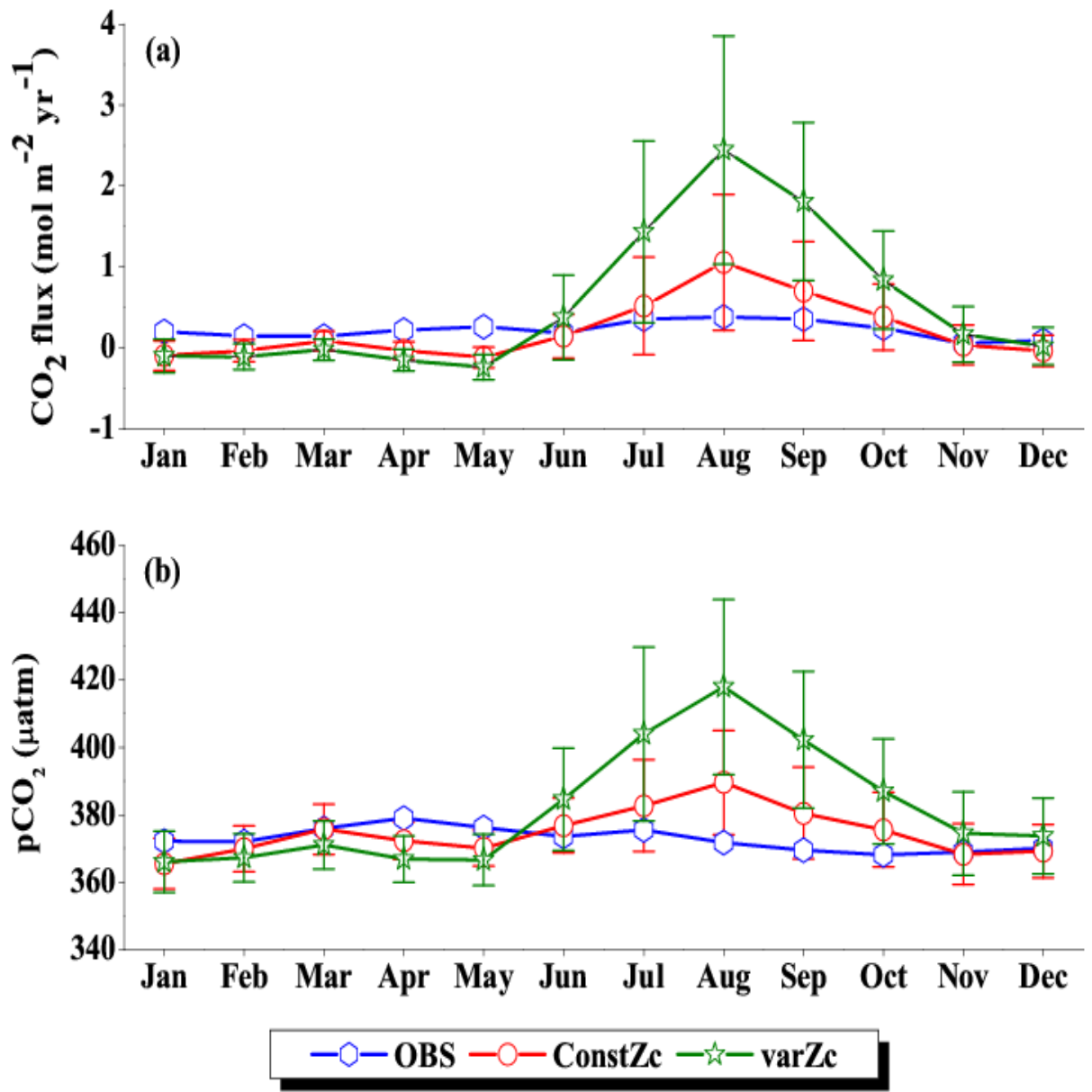


Figure 12: Same as Figure (6), but for SC.

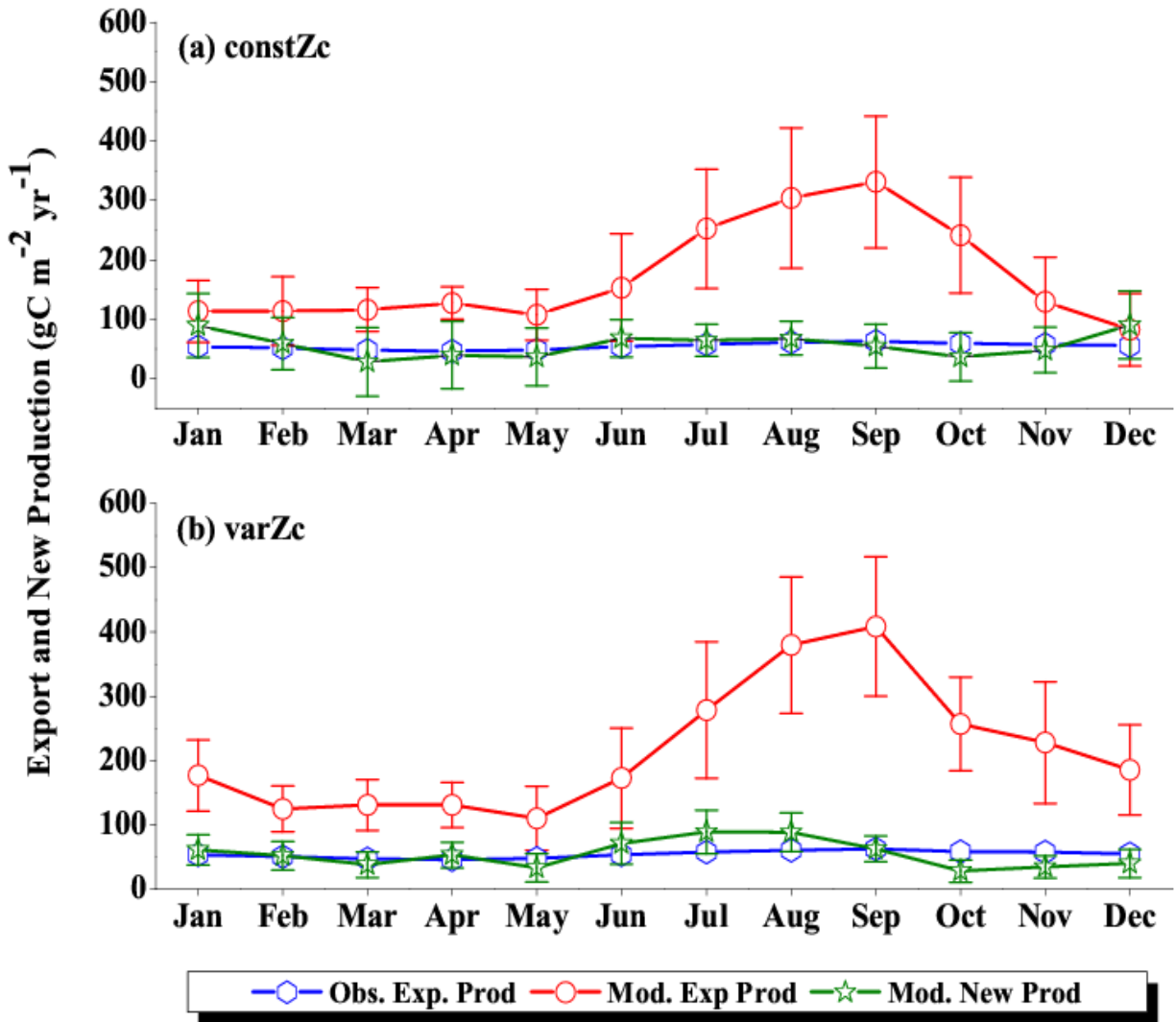


Figure 13: Same as Figure (7), but for SC.

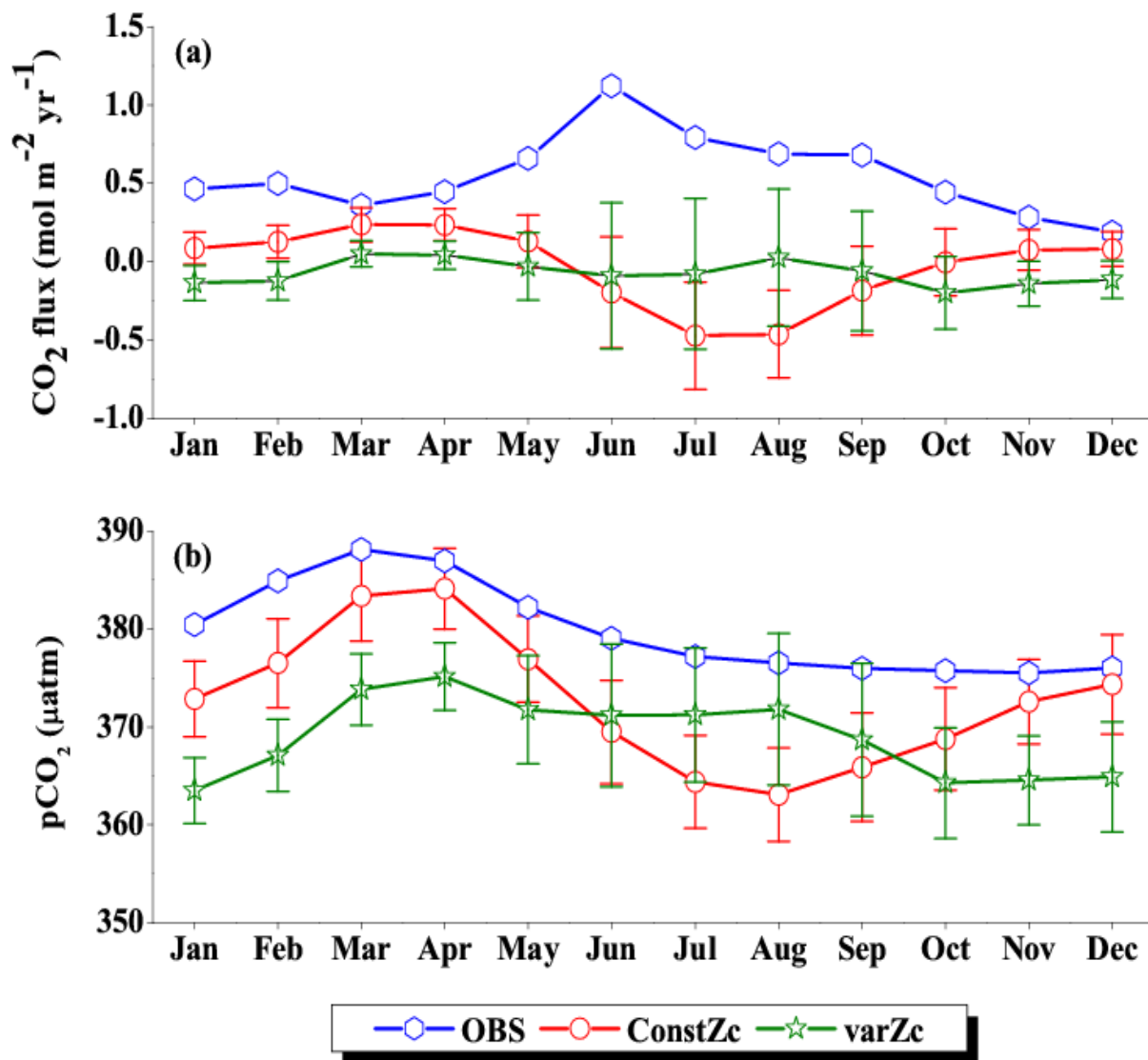


Figure 14: Same as Figure (6), but for SCTR.

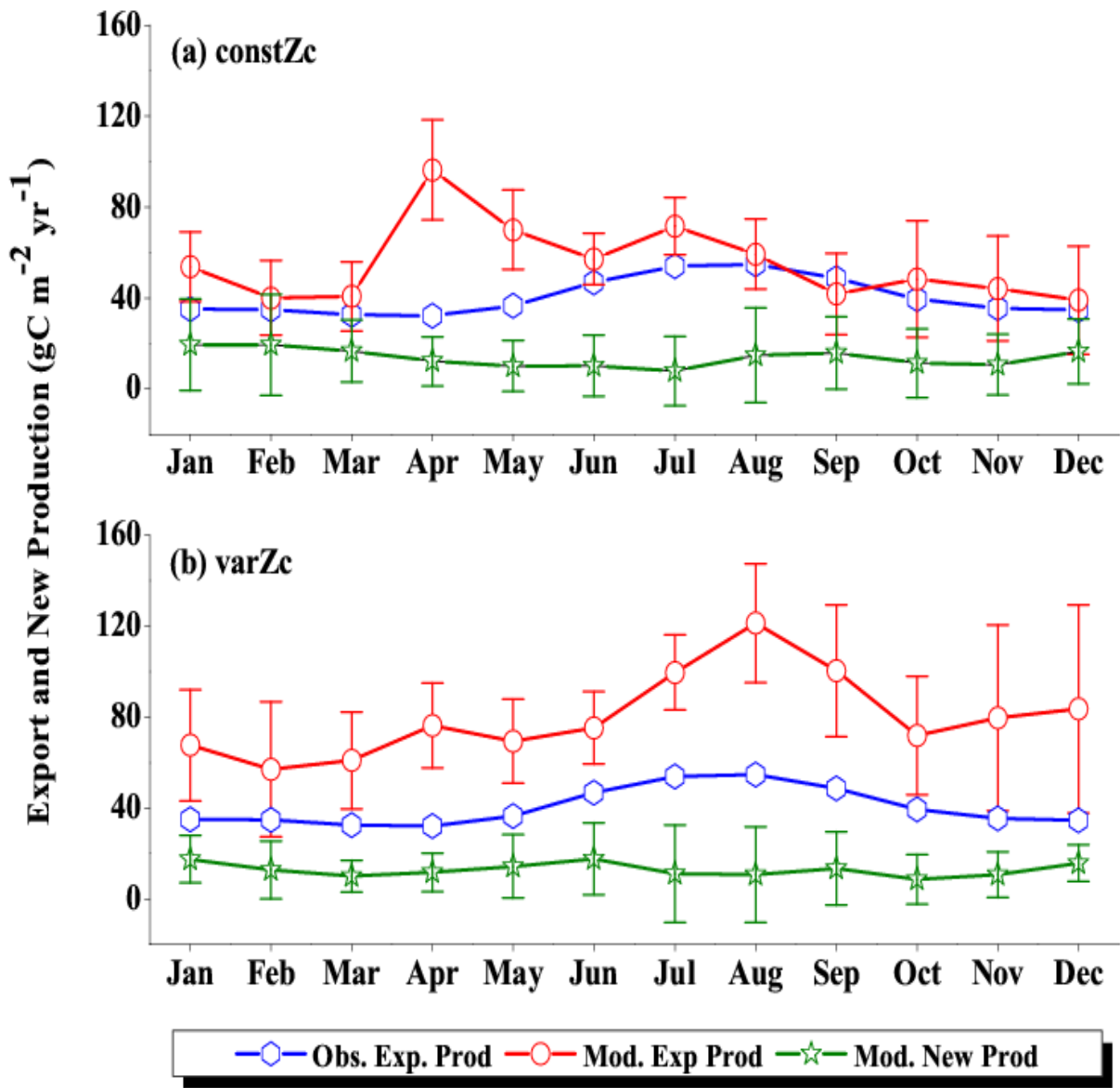


Figure 15: Same as Figure (7), but for SCTR.

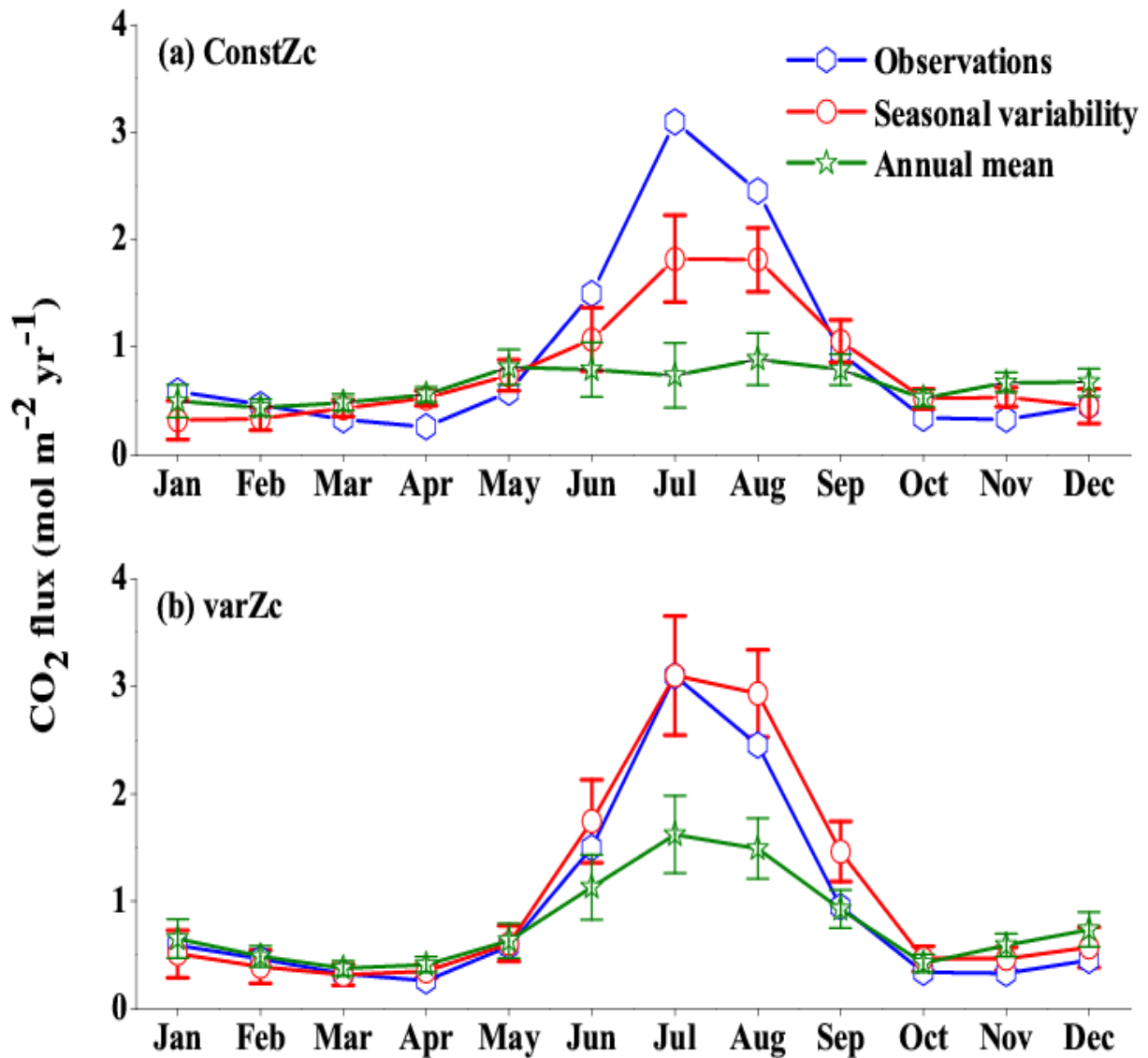


Figure 16: Response of CO₂ flux from the model forced with annual mean currents over the WAS as climatology computed over 1990-2010. Error bar shows standard deviations of individual months over these years. (a) constZc and (b) varZc. Units are mol m⁻² yr⁻¹. Legends are same for both graphs.

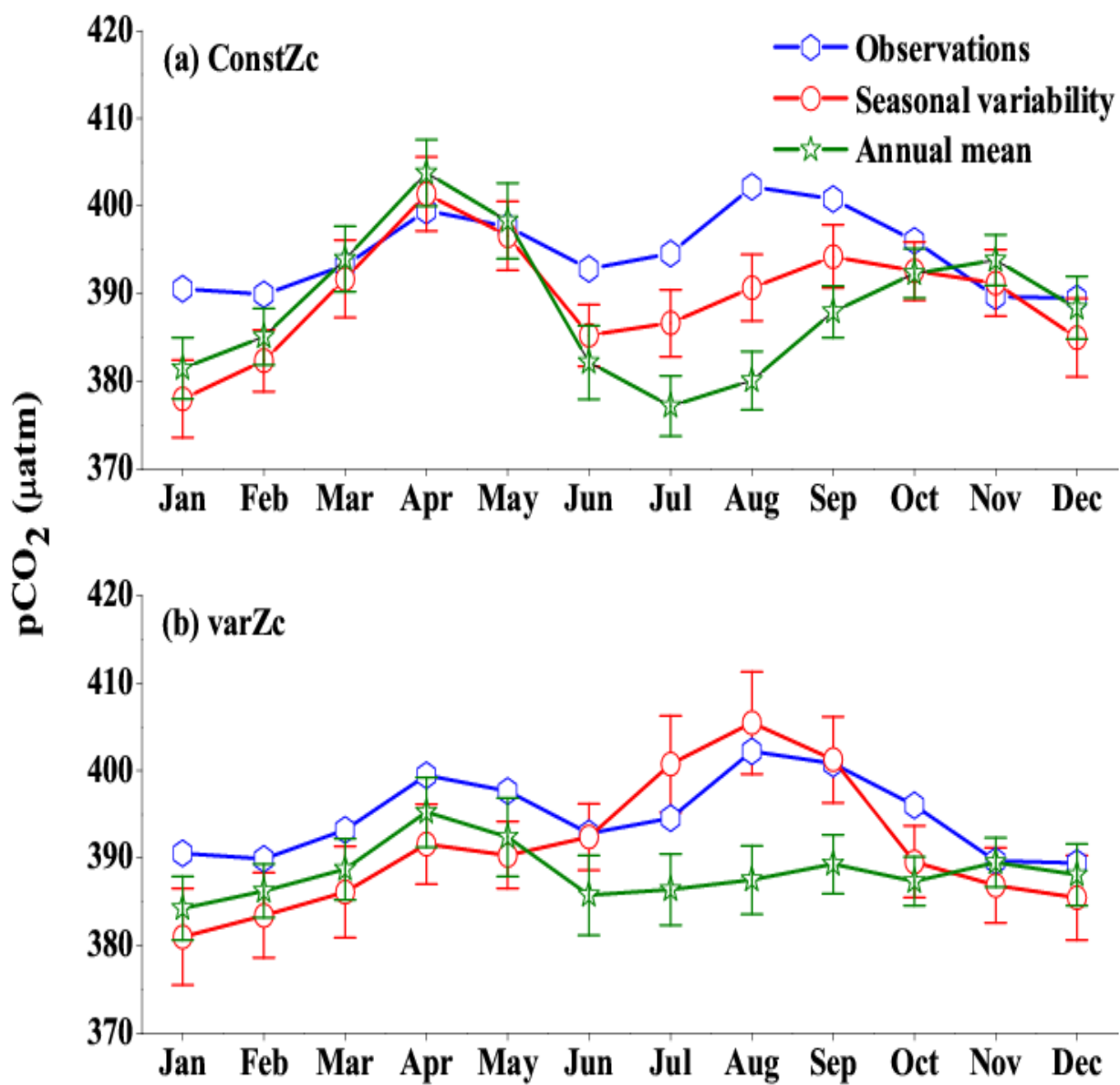


Figure 17: Same as Figure (16), but for pCO₂. Units are µatm.

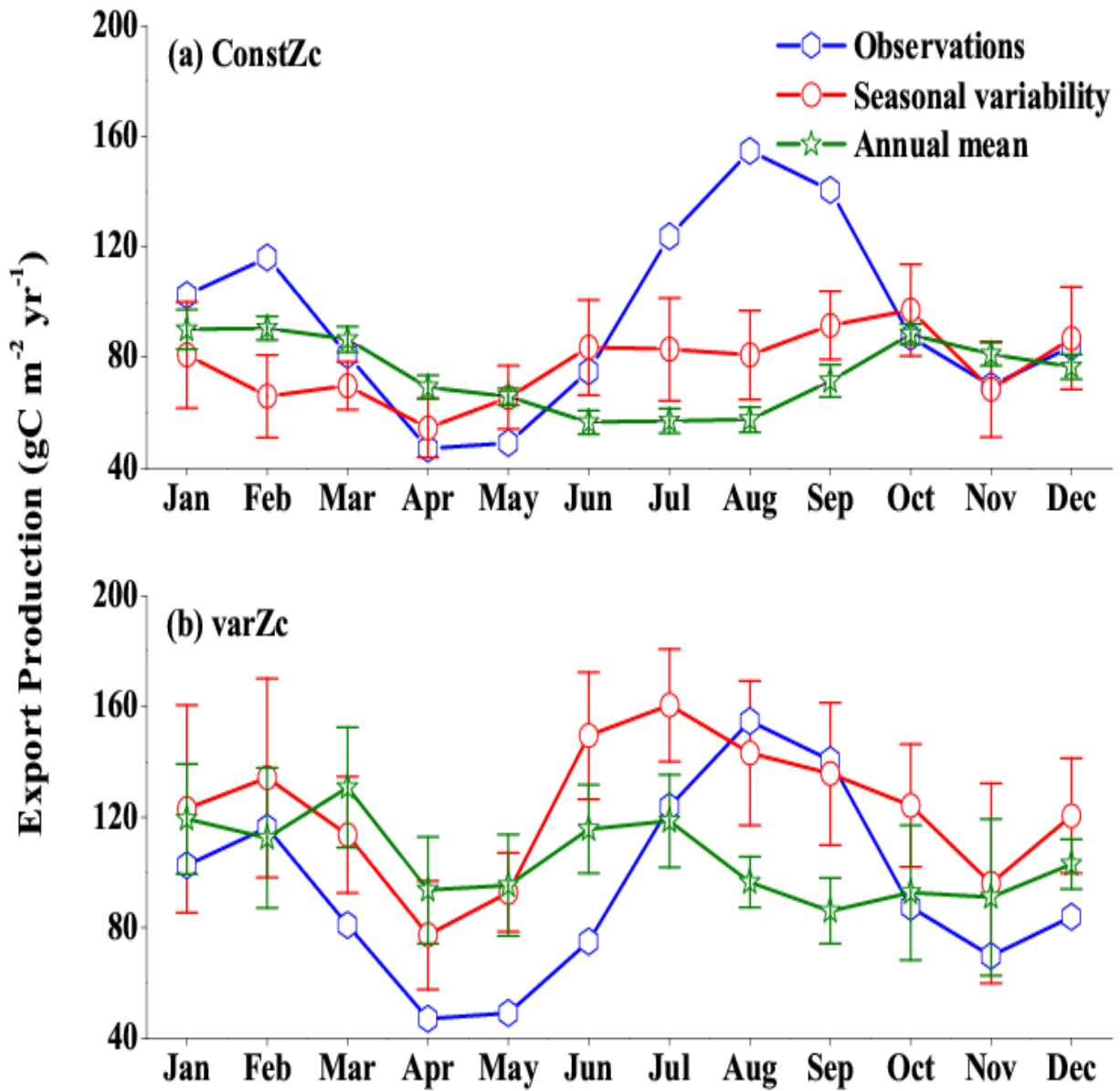


Figure 18: Response in the export production of the model forced with annual mean currents in the WAS as climatology computed over 1990-2010. Error bar shows standard deviations of individual months over these years. (a) constZc (b) varZc. Units are $\text{g C m}^{-2} \text{ yr}^{-1}$. Legends are same for both graphs.

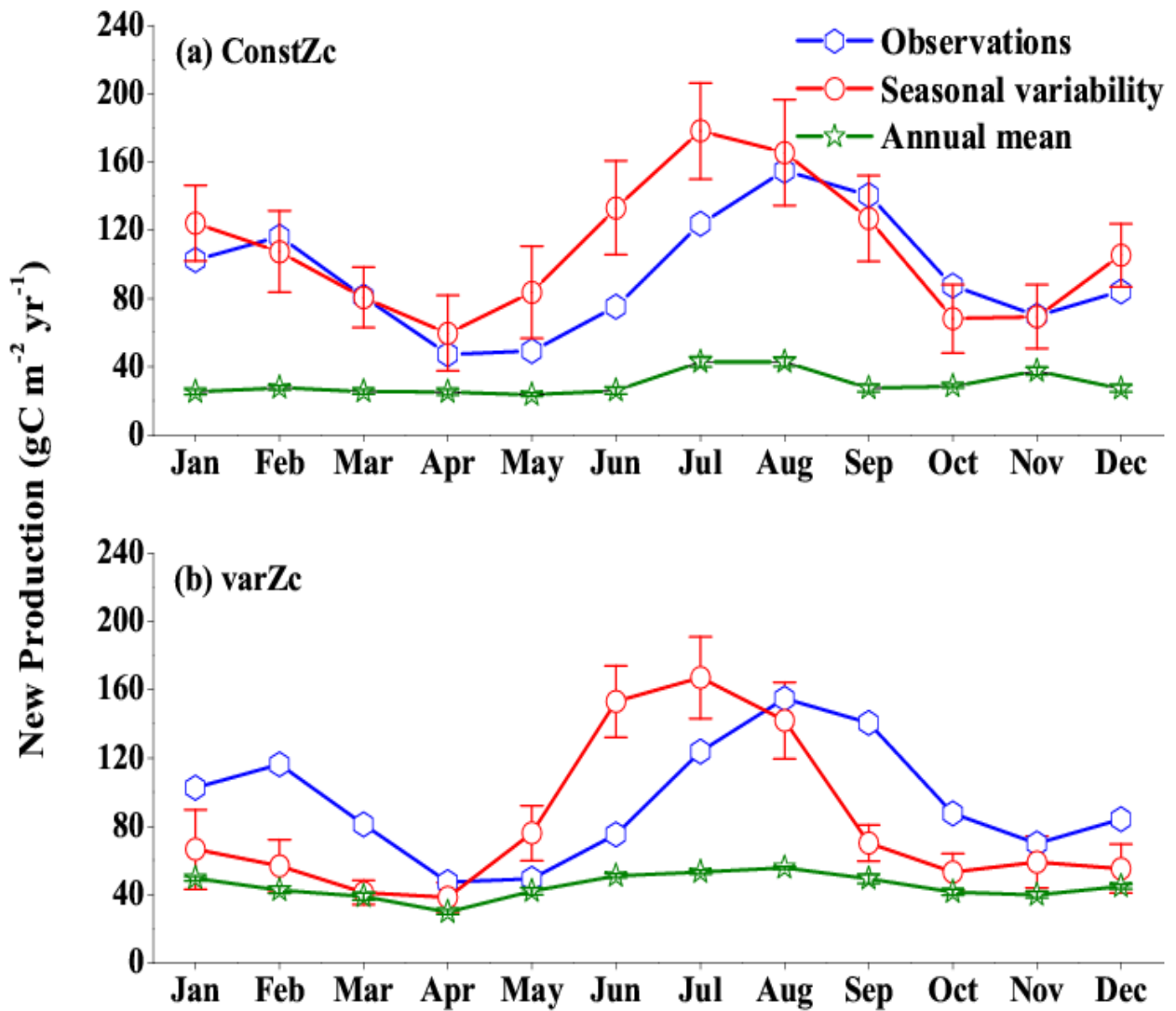


Figure 19: Same as Figure (18), but for New Production. Units are g C m⁻² yr⁻¹.

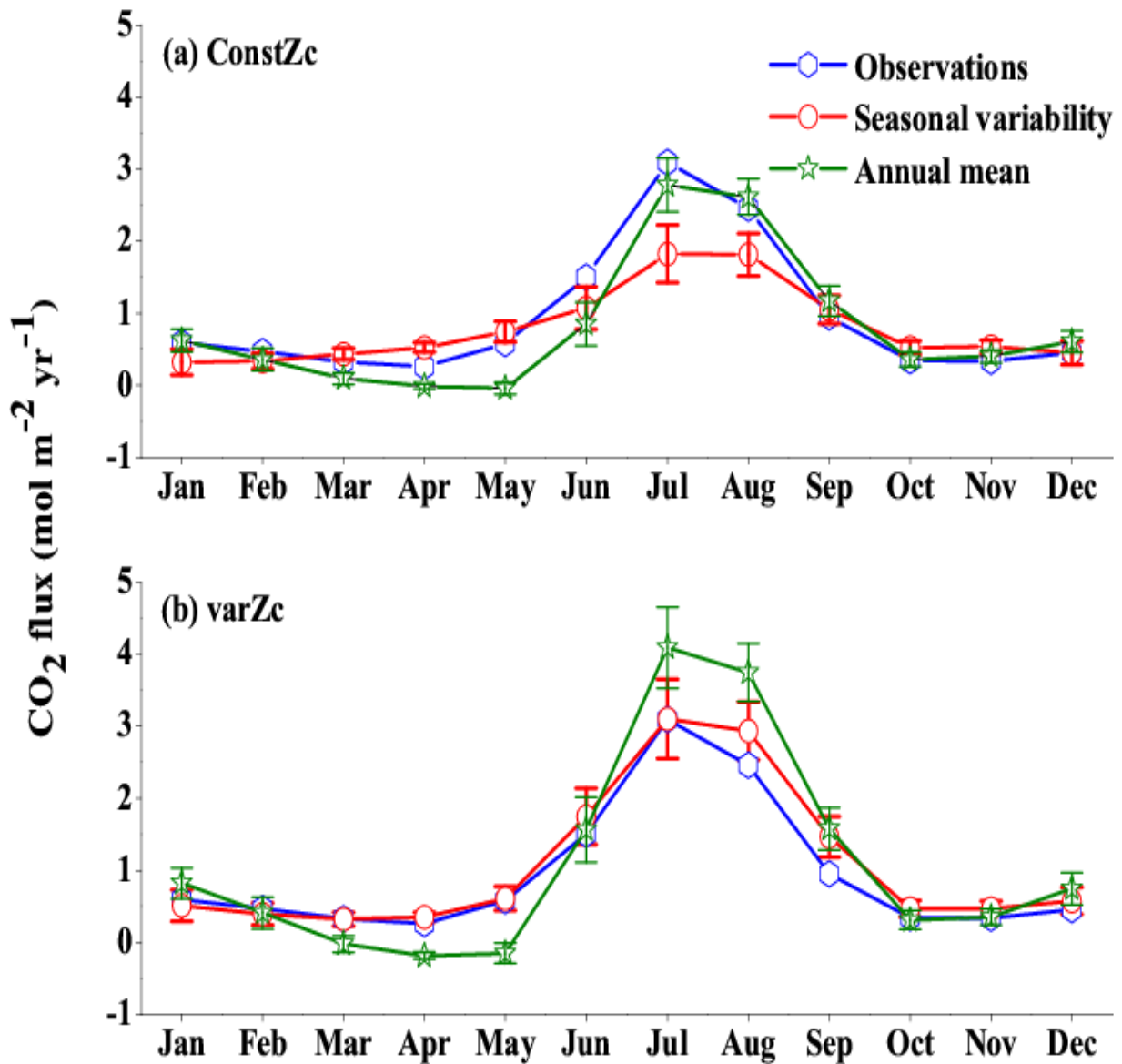


Figure 20: Response of CO₂ flux from the model forced with annual mean SST over the WAS as climatology computed over 1990-2010. Error bar shows standard deviations of individual months over these years. (a) constZc and (b) varZc. Units are mol m⁻² yr⁻¹. Legends are same for both graphs.

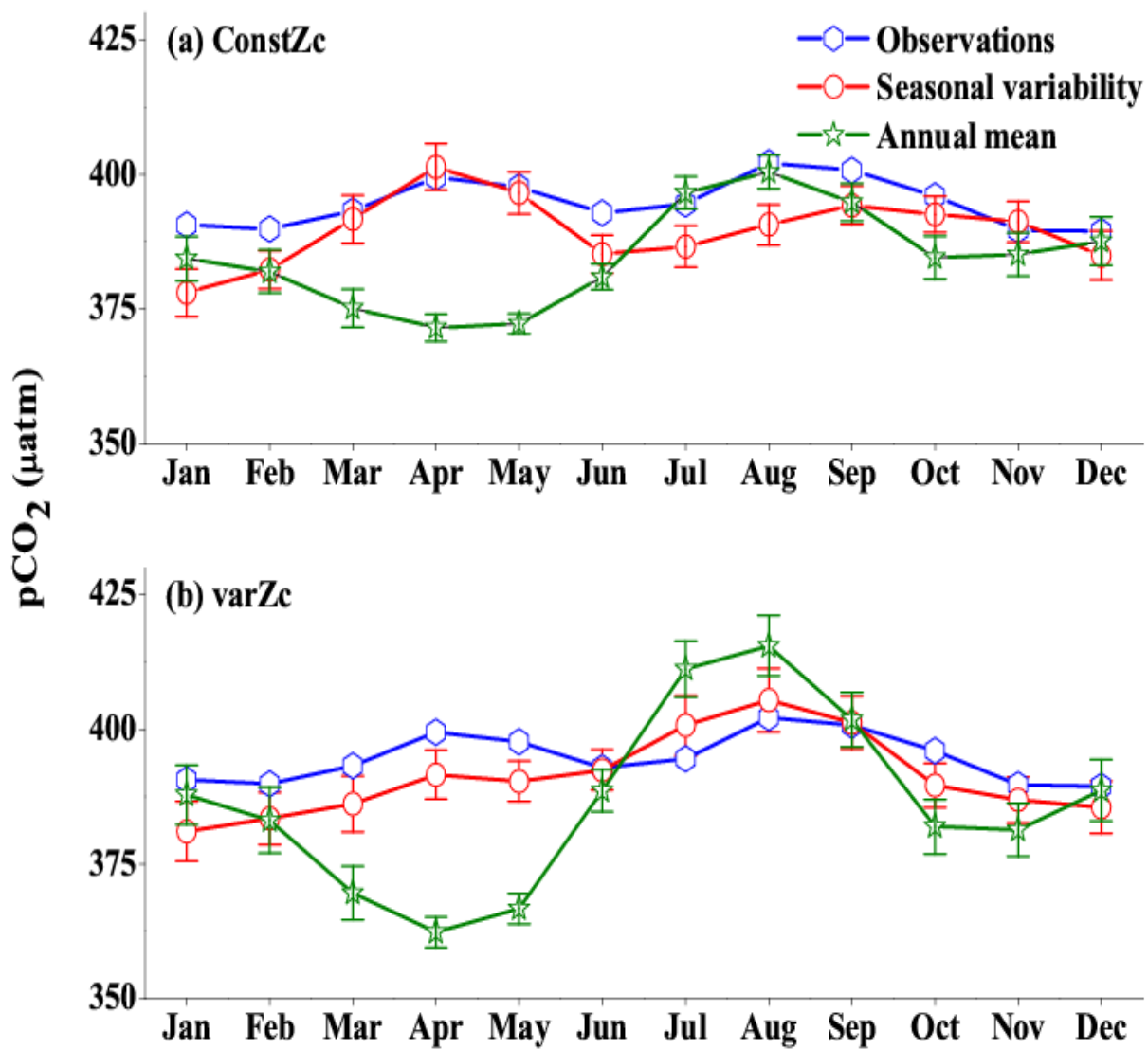


Figure 21: Same as Figure (20), But for $p\text{CO}_2$. Units are μatm .